www.sciencemag.org/cgi/content/full/330/6004/646/DC1

Supporting Online Material for

Rate of Gas Phase Association of Hydroxyl Radical and Nitrogen Dioxide

Andrew K. Mollner, Sivakumaran Valluvadasan, Lin Feng, Matthew K. Sprague, Mitchio Okumura,* Daniel B. Milligan, William J. Bloss, Stanley P. Sander,* Philip T. Martien, Robert A. Harley,* Anne B. McCoy,* William P. L. Carter*

*To whom correspondence should be addressed. E-mail: mo@caltech.edu (M.O.); stanley.p.sander@jpl.nasa.gov (S.P.S.), harley@ce.berkeley.edu (R.A.H.); mccoy@chemistry.ohio-state.edu (A.B.M.); wpcarter@ucr.edu (W.P.L.C.)

Published 29 October 2010, *Science* **330**, 646 (2010)
DOI: 10.1126/science.1193030

This PDF file includes:

SUPPORTING ONLINE MATERIAL

Rate of Gas Phase Association of Hydroxyl Radical and Nitrogen Dioxide

Andrew K. Mollner[1], Sivakumaran Valluvadasan[2], Lin Feng[1], Matthew K. Sprague[1], Mitchio Okumura[1], Daniel B. Milligan[2], William J. Bloss[2], Stanley P. Sander[2], Philip T. Martien[3], Robert A. Harley[3], Anne B. McCoy[4], William P. L. Carter[5]

[1] *Arthur Amos Noyes Laboratory of Chemical Physics, Division of Chemistry and Chemical Engineering, California Institute of Technology, Pasadena, CA 91125, USA*
[2] *Jet Propulsion Laboratory, California Institute of Technology, Pasadena, CA 91109, USA*
[3] *Department of Civil and Environmental Engineering, University of California, Berkeley, CA 94720-1710, USA*
[4] *Department of Chemistry, The Ohio State University. Columbus, OH 43210, USA*
[5] *College of Engineering, Center for Environmental Research & Technology, University of California, Riverside, CA 92521 USA*

CONTENTS:

I. Materials and Methods

a. Termolecular Reaction Kinetics

The effective bimolecular rate constant for a termolecular association reaction (such as reactions 1a and 1b in the main text) increases monotonically but nonlinearly with pressure and can be described by the Lindemann-Hinshelwood mechanism (*S1-S3*). The rate constant varies linearly with buffer gas pressure in the low pressure limit but asymptotically approaches a constant value and becomes independent of pressure in the high-pressure limit. This pressure dependence is known as the fall-off curve and given by (*S1-S2*)

$$k([\mathrm{M}]) = \left(\frac{k^0[\mathrm{M}]}{1 + \frac{k^0[\mathrm{M}]}{k^\infty}} \right) F_c^{\left\{ 1 + \left[\log_{10}\left(\frac{k^0[\mathrm{M}]}{k^\infty} \right) \right]^2 \right\}^{-1}} \qquad \text{(S1)}$$

and is characterized by two parameters, the low-pressure limiting termolecular rate constant k^0 (cm^6 $molecule^{-2}$ s^{-1}) and the high-pressure-limit second-order rate constant k^∞ (cm^3 $molecule^{-1}$ s^{-1}). The rate constants k^0, k^∞, and k are all temperature dependent, but we have omitted the temperature dependence in this study, because all measurements were performed at 298 K. We fixed the parameter $F_c = 0.6$ as recommended in the NASA Jet Propulsion Laboratory (JPL) Chemical Kinetics Data Evaluation (*S4*).

Each of the rate constants for the two OH + NO_2 reaction channels 1a and 1b possesses an independent fall-off curve; therefore, the two sets of parameters (k^0_{1a}, k^∞_{1a}) and (k^0_{1b}, k^∞_{1b}) are independent and must be determined simultaneously. The strategy employed here is to measure the pressure dependences of the total rate constant

$k_1([M]) = k_{1a} + k_{1b}$

and the branching ratio of the rate constants

$\alpha([M]) = k_{1b}/k_{1a}$

and then to fit the two data sets simultaneously to obtain $k^0_{1a}, k^\infty_{1a}, k^0_{1b}$, and k^∞_{1b}.

Due to the limited range of pressures that we have measured, the derived fall-off curves are valid only in the pressure range studied (50-800 Torr); in particular, the derived values of the fall-off parameters are empirical, and care must be used in interpreting them beyond the intended range.

b. OH + NO_2 Kinetics

A schematic diagram of the PLP-LIF system to study OH + NO_2 kinetics is shown in Fig. S1. The experiments were carried out in an octagonal stainless steel reaction cell (20-cm inside diameter, 15-cm high) with four pairs of side ports. The pump beam (excimer laser) and probe beam (dye laser) crossed in the center of the cell. The laser beams entered the cell via antireflection-coated windows and passed through two pairs of perpendicular ports with long, baffled side-arms which were purged with flowing inert gas. A third pair of ports was used for gas inlet and outlet along with a thermocouple probe to measure the temperature of the gas in the cell. The fourth pair of ports was used for *in situ* measurement of the NO_2 concentration in the cell.

OH radicals were produced by the photolysis of $HONO_2$ at 248 nm (single pulse from KrF excimer laser)

$$HONO_2 + h\nu\ (248\ nm) \rightarrow OH\ (X^2\Pi, v = 0) + NO_2 \qquad (S2)$$

$HONO_2$ was transported to the photolysis cell by bubbling a 15-20 standard cubic centimeter per minute (sccm) flow of air, N_2, O_2 or He through neat anhydrous $HONO_2$ (prepared in the laboratory from the reaction of $NaNO_3$ and H_2SO_4) held in a trap. The primary impurity in the $HONO_2$ sample was NO_2. After the sample was purged by bubbling carrier gas through the trap the impurity NO_2 was less than 1%. The repetition rate of the photolysis laser was 20-30 Hz. Typically, an initial concentration of about 10^{15} $HONO_2$ cm^{-3} were photolyzed at a laser fluence of (0.6-1.1) mJ cm^{-2} to generate ≈ (5-10) × 10^{10} cm^{-3} of OH in each photolysis pulse.

The time-resolved OH signal was obtained by laser-induced fluorescence (LIF). Excitation of the $A^2\Sigma$ ($v = 1$) ← $X^2\Pi$ ($v = 0$), Q_{11} (1) transition at 281.997 nm was achieved using the frequency doubled emission from a diode-pumped solid state (DPSS)-pumped dye laser (Rhodamine 6G) operating at a pulse repetition rate of 10 kHz. Fluorescence from OH was collected by a lens and baffle system through a 308 nm interference filter and detected by a photomultiplier tube operating in photon counting mode. The collection optics were placed mutually perpendicular to the pump and probe beams that defined the interaction region. A concave mirror with an *f*-number matching the collection optics was placed in the bottom of the reaction cell to enhance the fluorescence collection efficiency and double the viewing solid angle for the

photomultiplier. The timing of the pump laser, probe laser, and multi-channel scaler were synchronized by digital delay generators.

The photon count vs. time was recorded by a multi-channel scaler board in a personal computer. In this way, an entire OH kinetic decay trace was recorded after each photolysis pulse. In many other PLP-LIF experiments, box-car averaging was used, i.e. for each laser shot the OH fluorescence signal was measured at a single fixed delay time with respect to the photolysis pulse using analog detection; the OH decay profile was then obtained by incrementing the delay between the photolysis and probe laser pulses. The combination of improved measurement duty cycle and photon counting in the present system resulted in enhanced detection sensitivity and reduced systematic errors. The enhanced sensitivity allowed us to extend measurement of rate coefficients to pressures above 700 Torr of air, at which OH fluorescence quenching is normally quite severe.

Observed OH decay profiles were fit to determine the pseudo-first-order rate constants, $k' = k_1[NO_2]$. The uncertainties of the fitted values of k' were on the order of 1% (1σ) or less.

Gas mixtures entered the mixing column ≈ 50 cm upstream of the photolysis region to ensure proper mixing of the gas. The pressure in the cell was monitored with 10 and 1000 Torr capacitance manometers over the range of 50 to 900 Torr of buffer gases (air, N_2, O_2 and He). The capacitance manometers were calibrated against secondary standards that were accurate to better than 1% (1σ). Typical flow rates, regulated using calibrated mass flow controllers, were between 500 and 1400 sccm, resulting in linear gas velocities in the reaction cell of > 50 cm s^{-1}. These conditions ensured that a fresh gas sample was photolyzed at each laser pulse and prevented build up of products.

NO_2 concentrations were typically 2-10$\times 10^{14}$ cm^{-3}, with concentrations measured by *in situ* absorption spectroscopy. The NO_2 absorption spectrum between 410-450 nm was recorded by a spectrograph/diode array system with a resolution of ~ 0.2 nm (Fig. S2). The concentrations were determined by least-squares fitting of the measured data to a reference UV absorption spectrum from Vandaele et al. (*S5*) and Nizkodorov et al. (*S6*), degraded to a spectral resolution of 0.2 nm. Fig. S2 shows the measured spectrum, scaled reference spectrum and fit residuals for a typical NO_2 concentration determination using the in-situ spectrometer. This method is more accurate than the NO_2 measurements made using absorption at a single wavelength as done in previous studies (*S7*-*S9*). The estimated uncertainty of the measured $[NO_2]$ was ≤ 3% (1σ), with the principal contribution to the uncertainty arising from uncertainties in the absorption cross sections of the reference spectrum.

At each pressure, 10 to 15 OH decay profiles were typically measured at various NO_2 concentrations. We calculated the effective bimolecular rate coefficient k_1 for each pressure from a linear fit of the k' dependence on the measured $[NO_2]$. Table S3 gives values of k_1 measured in air, N_2, and O_2.

The uncertainties reported in the table are the statistical uncertainties derived from the fits of k' as a function of $[NO_2]$. There is an additional systematic uncertainty from the uncertainty in the NO_2 cross section.

c. HOONO / $HONO_2$ Branching Ratio

Experiments to determine α were performed separately with a new apparatus. We used PLP to initiate reaction (1) by photolyzing precursors in a flow cell, combined with cavity ringdown spectroscopy (CRDS) to record absorption spectra of the primary reaction products. This apparatus had several advantages over the previous low pressure experiment done in our group on this reaction using a discharge-flow method to initiate reaction (1) (*S10*): PLP-initiation allowed real-time detection of intermediates and products with 10 μs time resolution, enabled reaction (1) to be studied at higher pressures (50-750 Torr) and minimized secondary and wall reactions. These developments were critical to the determination of the branching ratio under tropospheric conditions. In addition to these experimental modifications, we also better quantified the systematic deviations in the nitric acid absorption spectra resulting from the use of the CRDS method. Finally, we refined our theoretical modeling of the HOONO spectrum. These improvements allowed us to obtain more accurate branching ratio α estimates from the integrated intensities of the observed absorption bands.

(i) Generation and Detection of Products

A detailed schematic of the apparatus is shown in Fig. S3. The cell was a stainless steel rectangle 7.5 cm long with a 1 cm × 1 cm cross section and quartz windows on two sides for transverse pumping by the excimer radiation. The central axis of the cell was the path of the ringdown laser beam. The photolysis cell was sealed on each end to Teflon blocks which had feedthroughs for gas, pump-out and pressure readings. High reflectivity mirrors were sealed on either end to flanges and separated from the cell by 15-cm long purge volumes.The interior was coated with a thin Teflon film. The 70-200 mJ/pulse excimer beam was loosely focused to a rectangular spot typically 0.4 cm in height and 5 cm in length inside the cell.

We initiated the reaction OH + NO_2 + M by the photolysis of ozone by a 10 ns pulse of excimer radiation at 248 nm:

$$O_3 + h\nu(248nm) \rightarrow O(^1D) + O_2 \quad (S3)$$

$$O(^1D) + H_2 \rightarrow OH + H \quad (S4a)$$

$$H + NO_2 \rightarrow OH + NO \quad (S5)$$

$$OH + NO_2 + M \rightarrow HONO_2 + M \quad (1a)$$

$$\rightarrow HOONO + M \quad (1b)$$

This chemistry was modeled and found to be an efficient source of OH with few unwanted byproducts over a wide pressure range (100-750 Torr).

Initiating reaction (1) by this scheme required a system that was relatively free of O_2 to prevent the rapid formation of HO_2. As a result, the branching ratio measurements were all done in a buffer gas mixture of mostly N_2 with the remainder essentially all H_2.

All gas flows were measured by calibrated mass flow transducers (Edwards Model 831 and Omega Model 1700) and mixed in a glass cross about 5 cm prior to entering the photolysis region. Final concentrations of reactant gases in the photolysis cell were calculated from flows and pressures; typical gas concentrations can be found in Table S1. During experiments, reactant gas concentrations were varied systematically to check for any unexpected correlations. The total gas flow velocity ensured that the residence time was less than 100 ms, so that each photolysis pulse (10 Hz laser repetition rate) irradiated a fresh gas sample.

Hydrogen was introduced as a pure gas, while NO_2 was introduced as a 4% mixture in N_2 (Matheson). Ozone was produced from an ozonizer (Osmonics V10-0) and then trapped on silica gel (6-12 mesh) at –78°C. The ozone was then delivered to the cell by flowing nitrogen across the silica gel. Ozone concentrations, which were monitored by 254 nm absorbance in a quartz cell prior to mixing with other gases, remained constant over the duration of individual IR scans. Pressures were measured with capacitance manometers which had recently been calibrated against secondary calibration standards at JPL and were accurate to ±1% (1σ). At the excimer laser fluences used, typical OH concentrations were on the order of 10^{13} cm^{-3} over the photolysis length (5 cm).

Infrared absorption spectra were recorded by pulsed cavity ringdown spectroscopy. The ringdown apparatus has been described in detail previously (*S10*). A mid-infrared laser pulse was injected into an optical cavity made by the two high-reflectivity infrared mirrors (R = 99.98%, centered at λ = 2.8 μm, 6 m radius of curvature). The optical cavity length was approximately 50 cm, and typical ringdown lifetimes were 8 μs. Nitrogen (flow rate ≈10% of the total flow on each side) flowed over the mirrors and through the purge volumes to protect the mirrors and to minimize losses in reflectivity due to deposition.

Tunable mid-IR radiation (2.7-3.3 μm, pulse energy ≈1 mJ/pulse, linewidth ≈1 cm^{-1}, pulse width 5-6 ns) was produced by difference frequency mixing of the output of an Nd:YAG pumped dye laser with the 532 nm doubled-YAG beam in a two-stage potassium titanyl phosphate (KTP) Optical Parametric Amplifier (OPA) (*S11*). The residual beam exiting the cell was focused tightly onto a 1-mm diameter InSb detector (Infrared Associates). Each ringdown trace was amplified and then accumulated with a 50 MHz bandwidth 14-bit digitizer (GageScope 1450). For each point in a spectrum, 16 ringdown traces were averaged and then fit to a single exponential function and constant baseline by the Levenberg-Marquardt algorithm. We fit the first five lifetimes, but excluded the first microsecond due to electrical noise. The operation of the dye laser and OPA as well as the collection, averaging, and fitting of ringdown traces were controlled by a program written in Labview.

Absorption spectra were measured by the infrared probe laser 100 μs after the excimer laser pulse which generated radicals. This delay was sufficient for reaction (1) to go to completion, but short enough to minimize secondary reactions. Spectra were typically recorded by stepping the wavelength through the spectral region of interest. At each point, we alternated 16 shots with the excimer laser on with 16 shots with the excimer laser off. We then subtracted the two measurements to obtain spectra of reaction products. This subtraction eliminated background absorption due to species present in the absence of reaction, as well as the background arising from wavelength-dependent ringdown mirror loss.

A product spectrum ((excimer-on) − (excimer-off)) is shown in Fig. S4. All of the major features were attributed to absorption by $HONO_2$, HOONO, and nitrous acid (HONO). The production of HONO from the reaction of NO produced in reaction S5 with OH was unavoidable. The concentration of HONO was generally about 10% that of $HONO_2$ and did not impact our ability to integrate the HOONO and $HONO_2$ spectra. HONO and $HONO_2$ spectra were obtained from reference spectra and verified in the laboratory.

We obtained the *cis-cis* HOONO spectrum, shown in Fig. S5 after subtraction of underlying HONO and $HONO_2$ bands, from detailed studies under a variety of precursor conditions. The reported spectrum differs slightly from the previously reported work (*S10*), because we have improved the signal to noise and identified a long absorption tail to the blue, which we attribute to sequence bands (analysis will be described below). Only the *cis-cis* conformer of HOONO is observed in this region, due to an internal hydrogen bond which shifts the band center 250 cm^{-1} to the red from that of *trans-perp* HOONO (see discussion below regarding the spectrum of HOONO). *Cis-cis* HOONO is the most stable conformer and, on the time scale of these measurements, our measurements should represent the total amount of stabilized HOONO from reaction 1 (*S10, S12*).

As seen in Fig. S4, product spectra were dominated by the ν_1 $HONO_2$ band. This band is a relatively strong absorption (1000-2000 ppm at the peak) with resolvable rotational lines. For such spectra, Cavity Ringdown spectra recorded with broad-band lasers can exhibit nonlinearities when measuring intensities, due to well known linewidth effects. We found such nonlinearities when measuring the ν_1 $HONO_2$ bandshape and integrated absorbance, (but not the HOONO band, which is much weaker). Careful calibration experiments were conducted to quantify this nonlinearity as a function of nitric acid concentration and pressure. These experiments involved over 300 measurements of nitric acid CRDS spectra while quantifying the concentration of nitric acid through its UV absorbance. Nonlinearities were found to be less dramatic at higher pressure due to pressure-broadening. Observed ν_1 $HONO_2$ integrated absorbances were multiplied by calibration factors ranging from 1.15 at 750 Torr to 1.79 at 100 Torr.

During branching ratio measurements, product spectra were collected in about 30 minutes by scanning with a step-size of 1.5 cm^{-1}, a lower resolution than in Fig. S4, in order to minimize systematic errors due to long-term drift. Band contours in the product spectra were then determined by fitting the observed spectrum as a linear combination of the reference spectra for HOONO, $HONO_2$, and HONO recorded at high resolution. The ratio of the integrated intensities of the ν_1 HOONO band at 3306 cm^{-1} and the ν_1 $HONO_2$ band at 3550 cm^{-1} were then determined from the fitted weighting constants and the known integrated intensities of the reference spectra.

In principle, the presence of vibrationally excited OH (OH*) on the HOONO branching ratio measurements can affect the branching ratio. Both sources of OH, reactions S4a and S5, are known to produce OH* with significant population in $\nu > 1$ states. While collisional deactivation of OH* is efficient, collisions of hot OH with NO_2 may occur. NO_2 is known to be an efficient quencher ($k = 4.8\times10^{-11}$ cm^3 $molecule^{-1}$ s^{-1}) for excited OH (*S13*).

$$OH^* + NO_2 \rightarrow OH + NO_2^* \qquad (S6)$$

If, in addition to quenching, OH* can react with NO_2 to form products by

$$OH^* + NO_2 + M \rightarrow HONO_2 + M, \qquad (S7a)$$

$$OH^* + NO_2 + M \rightarrow HOONO + M, \qquad (S7b)$$

then reactions S7a and S7b compete with reactions 1a and 1b, leading to a higher effective temperature.

To examine the possible effect of vibrationally excited OH on our measurements of the branching ratio, we performed a set of control experiments using an alternate method for OH production with a substantially different (colder) nascent vibrational

distribution. We chose to use methane as the OH precursor rather than H_2, because the reaction

$$O(^1D) + CH_4 \rightarrow OH + CH_3 \quad \text{(S4b)}$$

produces OH*, but with a yield of OH with $v > 2$ that is much less than from reaction with H_2 (*S14, S15*). A careful examination of our observed HOONO/$HONO_2$ yields over the full pressure range showed no correlation between the source chemistry and the branching ratio, indicating that vibrationally excited OH* is not influencing our measured branching ratio.

(ii) Calculation of Branching Ratio

The measured integrated absorbances were converted to the ratio of HOONO/$HONO_2$ product concentrations, and thus $\alpha = k_{1b}/k_{1a}$, using the *ab initio* calculated ratio of v_1 band intensities:

$$\alpha([M]) = \frac{\int A_{HOONO}(v)\,dv}{\int A_{HONO_2}(v)\,dv} \times \frac{I_{HONO_2}}{I_{HOONO}} \quad \text{(S8)}$$

where $A(v)$ is the frequency dependent absorbance and I is the theoretical integrated or band intensity. These calculations of the ratio of the v_1 OH-stretch band intensities were carried out at a high level (CCSD(T)/ANO) and include both electronic and mechanical anharmonicities using second order vibrational perturbation theory (VPT2). The details of the method and results of these calculations for HOONO have been published previously (*S16*). Calculations for HOONO and $HONO_2$ yield a ratio of band intensities of

$$\frac{I_{HONO_2}}{I_{HOONO}} = 2.71 \quad \text{(S9)}$$

Previously published results on $HONO_2$ have shown intensity calculations done at this level of theory to be accurate to within 5% (*S17*). A comparison of this ratio of band intensities to that published previously at a lower level of theory (*S10*) shows that, while the calculated absolute intensities are highly dependent on the level of theory, the ratio of intensities is not. This suggests some cancellation of errors when taking the ratio of band intensities and gives us further confidence in the robustness of the ratio used here.

(iii) HOONO Torsional Excitation

As shown in Fig. S5, the v_1 band of HOONO has some intensity blue-shifted from the band origin at 3306 cm^{-1}. This intensity comes from HOONO molecules with excitation of low-lying torsional modes. Torsional excitation which breaks the hydrogen bond leads to blue-shifting of the OH stretch. This effect has been studied previously for the HOONO overtone spectrum (*S18, S19*). In order to quantify the amount of intensity shifted outside the spectrum shown in Fig. S5, a three-dimensional potential energy surface was calculated to investigate the impact of the HOON and ONOO torsions on the v_1 spectrum.

Since the ultimate goal of this calculation is to evaluate the band intensity in the HOONO fundamental that lies outside of the band region, we focused on a three-dimensional model of HOONO which included the OH stretch and the two lowest

frequency modes, the HOON and OONO torsion. We were comfortable leaving out the other six vibrations since an analysis of the anharmonicities reported by Matthews and Sinha (*S18*) showed their frequencies are not expected to shift substantially upon OH vibrational excitation. In contrast, we calculated the HOON torsion frequency to increase by 45 cm^{-1} when there is one quantum in the OH stretch compared to its value when the OH stretch is in its ground state. In addition, the normal mode vectors that describe the two lowest frequency modes both contain contributions from the HOON and OONO torsion. This is not surprising as the equilibrium configuration contains a hydrogen bond, and motion along either of these torsions will break the bond, leading to a response by the other torsion angle.

In order to construct the three-dimensional potential, we have selected a number of HOON and OONO torsion angles near the minimum energy geometry. We selected the angles to ensure that the potential was calculated over the full range that is sampled by the low-lying torsional levels. All of the points were calculated at the CCSD(T)/cc-pVTZ level of theory and basis and the energy was minimized with respect to the other seven internal coordinates. Once we had this two-dimensional surface, we evaluated the potential at eight additional points obtained by taking the geometries of the originally calculated points and increasing the OH bond distance by 0.25 Å and decreasing it by 0.15 Å in increments of 0.05 Å. The resulting 720 unique energies were then fit to a parameterized function of the OH bond distance, OONO angle and HOON angle that contains 79 parameters with an RMS error of 23.5 cm^{-1}. A more complete description of how this was achieved can be found in Ref. (*S20*) in which we fit a larger dataset of 1448 energies to 96 parameters, but in all other ways that calculation is identical to the one employed here.

Briefly, once we have the potential surface, energies and wave functions were determined in a two-step procedure. First, for a given value of the two torsion angles, we solved the one-dimensional Schrodinger equation for the energies and radial wave functions. The energies were then used to set up a two-dimensional Schrodinger equation for the torsion motions. This adiabatic approach was previously employed by Matthews and Sinha in a study of the OH/HOON torsion system (*S18*). We employed a fully coupled two-dimensional approach in our study of this sub-system, but found the differences between the results obtained by the two approaches were small (*S19*). Later studies also adiabatically separated the HOON torsion from the OH stretch (*S21*).

We evaluate the energies and wave functions from the two-dimensional torsion Hamiltonian, in a symmetrized basis of products of sine and cosine functions of the two angles. We include twenty-five sine and twenty-five cosine functions in the basis for each of the two angles. This ensures that the energies of the states of interest are converged to 0.01 cm^{-1}.

The calculated frequencies for the two states of interest to our measurements, $\nu_{OH}=0$ and $\nu_{OH}=1$ are shown in Table S2. The assignments were made based on the wavefunctions and the average kinetic energy of each torsion. The relative populations in the ground state, P_{Rel}, were calculated assuming a Boltzmann distribution

$$P_{\mathrm{Rel}} = \exp\left(\frac{-(E - ZPE)}{k_{\mathrm{B}}T}\right)$$

The blue-shift of each sequence band was calculated by comparing the ν_1=1←0 transition frequencies for states with torsional excitation to the transition frequency of the ground state.

The positions and relative intensities of the torsional hot bands are shown along with our measured HOONO spectrum in Fig. S5. This simulated spectrum reproduces the intensity seen to the blue of the main ν_1 band at 3370 cm^{-1} which stems from low amounts of excitation (mostly ≤ 1 quantum in the HOON torsion). In addition, there are many transitions with larger number of torsional quanta that are shifted farther to the blue than the region we have integrated. Due to their higher energy, however, these transitions have low population. At 298K, our calculated spectrum predicts that our integrated band includes 83% of the total HOONO intensity, with the remainder in sequence bands that are shifted above 3400 cm^{-1}. This has been used to correct our measured HOONO integrated absorbances to account for torsionally-excited molecules. We estimate the uncertainty in our measurements of α from this correction to be 5% (1σ).

d. Chemical Mechanism and Environmental Chamber Data

The SAPRC-07 (*S22, S23*) mechanism used in this study is version S07A (*S24*) without chlorine chemistry, including 74 species and 221 chemical reactions. Kinetic recommendations such as those compiled by the IUPAC and NASA/JPL panels and available kinetic and mechanistic data from other sources are very helpful in the development of chemical mechanisms used in atmospheric models. Simulations of environmental chamber data are also important because our knowledge of the details of the atmospheric reactions of many of the organic compounds emitted into the atmosphere is insufficient to derive predictive mechanisms. The development of the SAPRC-07 mechanism involved simulations of ~2400 environmental chamber experiments carried out in a number of chambers, with adjustments being made in uncertain portions of mechanisms for aromatics and a number of other VOCs based on these results (*S22, S23*). For this reason, changing an important rate constant such as k_{1a} in such a mechanism cannot be made without concern about how other aspects of the mechanism derived based on modeling chamber data may also be affected.

The SAPRC-07 mechanism as originally developed and evaluated used the NASA/JPL 2006 (*S4*) recommendation for k_{1a}, which gives a rate constant under atmospheric conditions that is 15% higher than that indicated by the results of this work. In order to assess whether modifying this rate constant would require other changes to the SAPRC-07 mechanism, we re-modeled the chamber data used in evaluating this mechanism using the revised value of k_{1a} developed in this work.

The set of environmental chamber experiments modeled, and the modeling methods, are the same as used when developing and evaluating the original SAPRC-07 mechanism (*S22, S23*), except that some outdoor chamber experiments not considered to be appropriate as a basis for adjusting the mechanism were not modeled. The only change to the gas-phase mechanism was that the parameters used to derive the rate constant for the reaction $OH+NO_2 \rightarrow HONO_2$ were changed from

$$k^0_{1a} = 1.80 \times 10^{-30} (T/300)^{-3} \text{ cm}^6 \text{ molec}^{-2} \text{ s}^{-1}; \; k^\infty_{1a} = 2.80 \times 10^{-11} \text{ cm}^3 \text{ molec}^{-1} \text{ s}^{-1},$$

the value recommended by JPL 2006 (*S4*) and used in the mechanism as originally developed, to

$k^0_{1a} = 1.48 \times 10^{-30}$ (T/300)$^{-3}$ cm^6 molec^{-2} s^{-1}; $k^\infty_{1a} = 2.58 \times 10^{-11}$ cm^3 molec^{-1} s^{-1}, which were derived based on the 298K values of k_{1a} developed in this work, but assuming the JPL 2006 (*S4*)-recommended temperature dependences. In both cases the JPL 2006 (*S4*) parameterization was used to derive the pressure dependence from k^0 and k^∞.

Evaluating mechanisms using environmental chamber data requires developing an ancillary model to represent chamber effects that must be appropriately represented when modeling chamber experiments (*S22, S23, S25*). One of the most important is the "chamber radical source" that takes into account the fact that radical levels in chamber experiments tend to be higher than can be accounted for by known gas-phase processes (*S26*). In the evaluation of SAPRC-07 this was represented in the chamber model by a light- and chamber-dependent out-gassing of HONO, whose rapid photolysis results in formation of OH radicals, and whose rate is derived by modeling CO - NO_x and alkane - NO_x irradiations in the various chambers (*S22, S23, S25*). These experiments are used to characterize this effect because modeling those experiments is very sensitive to this "radical source" parameter, because the photolysis of the chamber-derived HONO is the major radical initiating process in these experiments. Since the OH + NO_2 reaction is a major radical termination process in these experiments, the radical source parameter that gives the best fit to the data in these characterization experiments, and therefore is used when modeling the other chamber runs for mechanism evaluation, is affected by changes in this rate constant. If this is the dominant process affecting termination, the best fit radical source parameters should change by about the same factor as the change in the OH + NO_2 rate constant, or 0.873. Therefore most of the chamber modeling with the revised value of k_{1a} was done with the radical source parameter reduced by this factor.

II. Text

a. Experimental Results

Using the PLP-LIF apparatus, we measured the total rate coefficient k_1 for the reaction of OH with NO_2 in N_2, O_2, and air at buffer gas pressures up to 900 Torr (600 Torr for O_2). The results are given in Table S3 and displayed in Fig. 2A and Fig. S6. The rate coefficients k_1 in O_2 and air at a given pressure are lower than in N_2, because O_2 has a lower collision efficiency than N_2. Fig. S6 compares data taken in N_2, O_2, and air, along with a weighted average of N_2 and O_2 rate constants (weighted by the relative abundance in air). There is a slight systematic difference between the weighted average and the air measurements. The weighted average is higher than the measurements in air by an average additive constant of $0.35\times10^{-12} \pm 0.23$ (1σ) cm^3 s^{-1} at all pressures up to 600 Torr. A constant offset gave a statistically better correction than scaling over this pressure range. We selected as our best estimate for rate constants k_1 in air a set obtained by averaging the two results at each pressure. Rate constants k_1 in air at 700, 800 and 900 Torr were estimated with the additive correction described above.

Using the PLP-IRCRDS apparatus, we measured the branching ratio α at 298K in a mixture of N_2 and H_2 over the pressure range 20-760 Torr. While a total of 134 measurements were made, only a subset of 17 measurements with ≥90% N_2 over the range 100-760 Torr (Table S6) were used for the fits shown Fig. 2b and Fig. S7, due to uncertainty in the collision efficiency of H_2.

We used the two datasets, k_1 and α versus pressure, to determine fall-off parameters for the $HONO_2$ and HOONO channels (k^0_{1a} , k^∞_{1a}, k^0_{1b}, and k^∞_{1b}) for N_2 and air. We fit the data for k_1 and α simultaneously to the JPL formulation of the termolecular rate constant (F_c=0.6). Fits to the data are shown in Figs. S7-S9. Our best estimates of the parameters, given in Table S7, lead to the fall-off curves of the effective bimolecular rate coefficients k_{1a}, k_{1b} and k_1 shown in Fig. S10. These parameters are only valid within the pressure range studied, 100-800 Torr.

At low pressures, the association rate depends on the efficiency of the buffer gas to relax the complex. In determining the fall-off curves, relative differences in collisional relaxation can been accounted for by scaling the pressure by a parameter β, e.g. $[O_2] = \beta_{O_2} \times [N_2]$. We find that the coefficient $k_1^0(O_2)$ is lower than $k_1^0(N_2)$, in accord with previous results. Relative to nitrogen, we find $\beta_{O_2} = 0.63$ and $\beta_{air} = 0.92$, slightly lower than the earlier estimate obtained by Brown et al. ($\beta_{O_2} = 0.70 \pm 0.04$ and $\beta_{air} = 0.94 \pm 0.01$) (*S27*).

From our simultaneous fit to k_1 and α we obtain at 760 Torr(air) $k_1 = 10.57 \pm 0.08$ cm^3 $molec^{-1}$ s^{-1} and $\alpha = 0.142 \pm 0.002$, where the uncertainties are 1σ statistical uncertainties from the fit. In addition, each data set has several possible systematic errors. The k_1 data has 1σ uncertainties of 3% from the cross section of NO_2, and a 1% uncertainty in the pressure calibration which translates to a 0.5% uncertainty in k_1. The α data has 1σ uncertainties of 5% in the relative $HONO_2$ and HOONO intensities, 5% in the correction for torsional hot bands, and a 1% uncertainty in the pressure calibration which translates to a 0.5% uncertainty in α. Adding the systematic uncertainties in quadrature and then combining with the uncertainty in the fit leads to 1σ uncertainties of $k_1 = 10.57 \pm 0.48$ cm^3 $molec^{-1}$ s^{-1} and $\alpha = 0.142 \pm 0.012$. The final value of the rate coefficient for the nitric acid channel at 760 Torr air is $k_{1a} = 9.2 \pm 0.4$ cm^3 $molec^{-1}$ s^{-1}, with 1σ uncertainty calculated by standard propagation of errors.

b. Discussion of the Total OH + NO_2 Reaction Rate Constant

There have been several experimental measurements of the total rate coefficient k_1 in pure nitrogen, but only four above 200 Torr (see Fig S8a). Table S4 summarizes the methods and pressures used in previous measurements of k_1 below 900 Torr. The results above 200 Torr fall into two ranges. Experiments by Anastasi and Smith (*S28*) and more recently by D'Ottone et al. (*S9*) measured the rate constant at pressures up to 500 and 700 Torr respectively. Their results agree well. However, Donahue (*S7*) and Dransfield (*S54*) measured rate coefficients up to 600 Torr that were lower by a factor of approximately two. Those experiments (*S7, S54*), with larger uncertainties at the higher pressures, were performed in a High Pressure Flow System (HPFS), a fast discharge flow (10 m/s) tube with OH fluorescence detection measured downstream from an OH injector.

An important difference between the HPFS experiment and the other measurements lies in the measurement times, 20-100 ms, much longer than the other experiments. It is conceivable that on this longer timescale the product HOONO could redissociate, regenerating OH and leading to a lower apparent rate (effectively k_{1a}). However, the lifetime of HOONO due to collisional dissociation, $\tau(\text{HOONO}) = k_{-1b} = k_{1b} / K_{eq}$, can be estimated from the best known values of equilibrium constant K_{eq} and k_{1b} .

Using the values given in JPL 2006, we find that is roughly one to two orders of magnitude longer than the residence time over the pressure range studied in the HPFS experiment at room temperature. Furthermore, HOONO redissociation alone could not account for the magnitude of the difference, unless the yield of the HOONO channel were substantially higher. Surface collisions or other uncontrolled variables may lead to HOONO loss (back to OH) or some other OH regeneration, but the cause of the discrepancy remains unknown.

Our results in N_2 (Fig. S8a) are consistent with the higher set of reported k_1 values, those of D'Ottone et al. (*S9*) and of Anastasi and Smith (*S28*), and disagree with the lower rate coefficients determined by the HPFS measurements (*S7, S54*). Closer inspection indicates that the fall-off curve fit to the current measurements give k_1 values slightly lower (≈10-20%) than D'Ottone et al. and Anastasi and Smith, outside the reported uncertainties.

Fig. S9 shows that our data in air is systematically slightly lower than the previous air measurements by D'Ottone et al., (*S9*) which arises from both lower k_1 observed in N_2 and a lower effective collisional efficiency (β) for O_2.

A significant source of systematic error arises from measurements of the NO_2 concentration used to convert pseudo-first order rate constants to bimolecular rate coefficients. The work of D'Ottone et al. (*S9*) are the only experiments to measure NO_2 in situ (using a single wavelength of 365 nm), measurements which are corroborated by pre- and post-cell measurements and flow calculations. In situ recording of a portion of the NO_2 spectrum, as shown in Fig. S2, provides a more robust measurement of NO_2. The current work is also the first to rely on re-measured absorption cross-sections determined by Nizkorodov et al (*S6*). Fig. S8b compares our k_1 data in N_2 with values from several model calculations fit to earlier data, and to the IUPAC and JPL 2006 recommendations. The best fit to our data lies slightly lower than the recommended fall-off curves.

In addition to systematic errors in determining NO_2 concentrations, measurements of rates are more difficult in O_2, which is an efficient quencher of OH fluorescence. The current experiment provides enhanced sensitivity to better overcome the drop in signal-to-noise.

c. Discussion of the HOONO/$HONO_2$ Branching Ratio

The current experiment provides a direct experimental determination of the product branching ratio, obtained by detecting both products *cis-cis*-HOONO and $HONO_2$ with the same method on short timescales over a wide range of pressures. Only the *cis-cis* isomer of HOONO is detected; however, while both the *trans-perp* and *cis-cis* forms of HOONO are formed initially, all HOONO should relax and isomerize to the lowest-energy *cis-cis* prior to our spectroscopic measurements (*S12*). Measurement within 100 μs minimizes interferences and biases from secondary reactions. The determination of α relies on theory only for the ratio of HOONO and $HONO_2$ absorption cross-sections, which have been calculated at very high levels of theory and seems robust with level of theory, and for the correction due to the shifting of sequence bands. State-of-the-art theoretical methods allow us to determine these with high confidence for small closed-shell molecules such as these.

While the HOONO channel in the reaction OH + NO_2 was widely debated for many years, its existence is now supported by a large body of evidence (*S8, S10, S12, S21, S29-S33*) (*n.b.* – we report branching ratio as $\alpha = k_{1b}/k_{1a}$, and the yield or branching fraction for the HOONO channel as $k_{1b}/(k_{1a}, + k_{1b})$.

There have been several previous measurements and calculations of α, but only at conditions quite removed from those found in the atmosphere (Table S5). At very high temperatures and pressures the HOONO dissociation lifetime is much shorter. This has been observed in the form of bi-exponential OH decays by Hippler et al. and D'Ottone et al. (*S8, S30, S31*) These decays were fit to extract the rate constants k_{1a} and k_{1b} as well as the equilibrium constant K_{1b}. Hippler et al. measured $k_{1b}/k_{1a} = 0.15$ at 430 K and 3750 Torr He, with a HOONO dissociation rate of 20 μs (*S31*). D'Ottone et al. measured $\alpha = 0.11 \pm 0.03$ at 413 K and 400 Torr He, with a HOONO dissociation rate of 200 μs (*S8*). At 100 μs when we make our measurements at the lower temperature of 298 K, HOONO dissociation should be negligible. Since the lifetime of HOONO in the lower atmosphere is expected to be on the order of seconds (*S4, S29*), we have not included reaction 1b explicitly in the chemical mechanism.

At lower temperatures, there have also only been a few estimates of α, all at very low pressures. Donahue et al. measured the rate of ^{18}OH scrambling in the OH + NO_2 reaction in N_2. From this, they estimated the branching ratio in the low-pressure limit to be $\alpha = 0.17$ (*S29*), which is considerably higher than any other estimates of the low pressure branching ratio.

Nizkorodov and Wennberg made the first spectroscopic detection of HOONO, using overtone action spectroscopy. Although there were several unknown parameters (e.g. dissociation yield, absorption cross-section), they arrived at what is in retrospect an accurate estimate of the branching ratio $\alpha = 0.05 \pm 0.03$ at 253 K and 20 Torr (*S32*).

The current results are an advance over a previous cavity ringdown measurement of α in a low pressure discharge by some of the authors of this manuscript (*S10*). If we apply the improvements in analysis of the spectra of HOONO and $HONO_2$ described in this work, the published branching ratio should be revised to $\alpha = 0.048 \pm 0.013$ at 298 K and 20 Torr He/Ar/N_2. In a time-dependent capture theory study using a new restricted dimension ab initio potential energy surface, Williams et al. calculated $\alpha = 0.051$ at 20 Torr and 300 K and a similar temperature-dependence to that shown in the early discharge-flow experiment (*S34*).

Several studies have calculated values of the branching ratio (*S30, S34-S39*). Comparisons with predicted fall-off curves are shown in Fig. S7. The final fitted fall-off curves for the two channels 1a and 1b, obtained from the parameters given in Table S7, are plotted in Fig. S10. As predicted by earlier models, the HOONO channel is still predominantly in the low-pressure limit, i.e. it increases linearly with [M]. Much of the increase in the branching ratio with pressure thus comes from the fall-off in k_{1a} with pressure.

Early calculations, either pure RRKM calculations or RRKM calculations modified to fit the existing data, produced widely varying estimates of the branching ratio at 760 Torr: 0.1 (*S38*), <0.03 (*S39*), and 0.3 (*S37*). Much of the discrepancy could be attributed to poor knowledge of the energetics of HOONO, which have a large effect on the branching ratio. Recent calculations that take advantage of the more detailed knowledge of the potential energy surface, and new additions to the kinetics data set are more

consistent, as can be seen in Fig. S7. The results of Golden et al. (*S36*) and Hippler et al. (*S30*) are shown along with the NASA-JPL 2006 kinetics data evaluation recommendation (*S4*) in Fig. S7 (the IUPAC kinetics data evaluation currently contains no recommendation for the inclusion of reaction 1b (*S40*)). The calculations of Hippler et al. are in excellent agreement with the current measurements.

We assume that any HOONO formed will persist in the time window of our experiment but will redissociate to reactants OH + NO_2 in the atmosphere. At 760 Torr and 298K, the lifetime of HOONO with respect to collisional dissociation is τ(HOONO) = $k_{-1b} = k_{1b} / K_{eq}$ = 1.7 +1.7/-0.8 s, calculated from the equilibrium constant K_{eq} and k_{1b} given in JPL 2006, validating our assumptions. At significantly lower temperatures, e.g. in the free troposphere, the lifetime is likely to be long enough that the fate of HOONO must be considered.

Finally, it should be noted that Zhang et al. in an RRKM master equation modeling study suggested that *trans-perp* HOONO may have a concerted mechanism to isomerize preferentially to nitric acid (*S41*). They hypothesized the existence of an isomerization transition state with a barrier height lying well below the dissociation energy to account for recent experimental observations of nitric acid formation from the reaction HO_2 + NO. If it existed, such an isomerization pathway could lead to conversion of HOONO to $HONO_2$ instead of redissociation. However, earlier calculations found only transition states for concerted isomerization of *trans-perp* HOONO to $HONO_2$ that lay 1.5-3 kcal mol^{-1} above the barrier for dissociation to OH + NO_2) (*S42-S46*), and their structures were close to that of the nitric acid product, making direct isomerization of HOONO to $HONO_2$ much less likely than direct dissociation to OH + NO_2 (*S47*). More recently, Chen et al (*S48, S49*) found a weakly hydrogen bonded transition state that lies 0.7 kcal/mol below the dissociation limit; however, in performing quasiclassical trajectories, they find that trajectories that isomerize from HOONO to $HONO_2$ are rare, as expected from statistical rate considerations: In thermal collisions, entropic factors will strongly favor simple bond fission over passage through a tight, concerted transition state, even if the latter is slightly below the dissociation limit.

d. Chemical Mechanism and Environmental Chamber Data

Fig. S11 shows plots of the average model errors in the simulations of ozone formed and NO oxidized for the various types of chamber experiments, for the SAPRC-07 mechanism as originally developed and for the mechanism with the lower k_{1a} obtained in this work. In this case model error is defined as {calculated $\Delta([O_3]–[NO])$ – experimental $\Delta([O_3]–[NO])$} / experimental $\Delta([O_3]–[NO])$, where $\Delta([O_3]–[NO])$ is the change in the quantity $[O_3]–[NO]$ during the course of the experiment. $\Delta([O_3]–[NO])$ is useful for assessing model performance in O_3 predictions in chamber experiments because it gives a measure of processes affecting ozone formation even when O_3 is suppressed by excess NO (*S25*). The standard deviations (1σ) of the averages are also shown, indicating the run to run variability of the fits of the model to the NO oxidation and O_3 formation data.

Fig. S11a shows that the original SAPRC-07 mechanism and chamber model has no bias in the simulations of the final $\Delta([O_3]–[NO])$ in the radical source characterization experiments, reflecting the fact that they were adjusted to fit these data. If only the OH+NO_2 rate constant is changed, then there is a slight positive bias of ~6% in the final

$\Delta([O_3]–[NO])$ simulations, but the bias is removed if the HONO offgasing parameter for all chambers is reduced by a factor of 0.87, the ratio of the change in the $OH+NO_2$ rate constants. This adjustment in the radical source parameters was used when simulating all the other experiments when using the new $OH+NO_2$ rate constant, since this is the appropriate chamber model to use with this revised mechanism.

Fig. S11b through Fig. S11d show average model errors for three representative types of experiments where the mechanisms were adjusted based on the simulations of the chamber data. In the case of the aromatics such as toluene and m-xylene, the quantum yields for the model species representing some of the photoreactive products were adjusted, and in the case of 1-butene and a number of other compounds the radical yields in the ozone reactions and the overall nitrate yield in the peroxy + NO reactions were adjusted. It can be seen that the mechanism with the reduced $OH + NO_2$ rate constant (and modified chamber model) does affect the results somewhat, though the effect is relatively small, especially at the end of the experiments. The results do not indicate any need to revise the mechanisms for these compounds, and this was also found to be the case for other aromatics and alkenes whose mechanisms were adjusted.

Mechanisms for alkanes and other compounds that do not have significant radical sources in their mechanisms cannot be evaluated by modeling compound - NO_x - air irradiations because such experiments are too sensitive to the chamber radical source (*S22, S23, S25, S26*). Instead, these mechanisms are evaluated by modeling "incremental reactivity" experiments, where the effects of adding the compounds to surrogate - NO_x - air irradiations are measured, and where the "surrogate" is a mixture of VOCs designed to approximately represent those present in ambient air (*S22, S23, S50, S51*). The performance of the mechanism is evaluated based on its ability to predict the incremental reactivities of the compounds relative to $\Delta([O_3]–[NO])$ and integrated OH radicals, where incremental reactivities are defined as the changes in the measured quantities caused by adding the test compound, divided by the amount added. (Integrated OH radicals are derived from rates of consumption of m-xylene that is present in the surrogate mixture used in the experiments.) Although mechanisms were not adjusted for most alkanes, adjustments for mechanisms were made for some other compounds based on results of incremental reactivity experiments, usually involving nitrate yields in peroxy + NO reactions. It was found that the effect of changing the $OH+NO_2$ rate constant on such incremental reactivity results for such compounds was small, as shown on Fig. S12 for representative alkane experiments. Therefore, adjustments of mechanisms based on such experiments should not be significantly affected by the change in $OH+NO_2$ rate constant.

Fig. S11e and Fig. S11f show average model errors for all of the single compound and all of the mixture experiments in the set of experiments used to evaluate the SAPRC-07 mechanism. In both cases the effects of changing the $OH+NO_2$ rate constant was small compared to the run to run variability. There was essentially no change in average bias by the end of the experiments for the single compound runs, though there was a slight positive change in the bias for the mixture experiments and in the initial stages of the single compound runs. There is no obvious way to change the mechanism to reduce biases in mixture experiments, and in any case the bias is relatively small.

These results indicate that there is no need to re-adjust the mechanisms for the major classes of compounds present in ambient air simulations as a result of changing the $OH+NO_2$ rate constant to the value derived in this work. There was a need to change the

chamber effects model when changing this rate constant, and this had to be done when modeling the mechanism evaluation data using the mechanism with the revised rate constant. However, this chamber effects model is not used in the ambient air simulations since they are assumed to reflect processes that need to be represented when modeling in environmental chamber experiments. The extent to which these processes occur in the atmosphere is uncertain, but in any case they are not represented in current models and if they were they would be derived using other methods than used when developing the chamber model.

e. Air Quality Modeling

We examined 8-h averaging times for O_3 concentrations, as the national ambient air quality standard for O_3 is now specified in terms of 8-h average values. The spatial distribution of predicted 8-h average ozone concentrations is shown in Fig. S13 for the base case (2010 emission inventory; SAPRC-07 mechanism with k_{1a} as recommended by NASA/JPL 2006). Ozone differences relative to this base case are also shown in the same fig. for lower (this work) and higher (IUPAC) values of k_{1a}. The spatial patterns in 8-h average ozone concentrations are the same as 1-h average midday values, and the effects on ozone of changes to k_{1a} considered here are similar over 8-h and 1-h averaging periods as well.

We also examined the impact of changes in k_{1a} upon OH, NO_2 and nitric acid. Maps of predicted concentrations of OH, NO_2, and nitric acid are shown in Figures S14-S16, respectively. Note in Figures S14a and S15a how high NO_2 concentrations in and around central Los Angeles inhibit OH radical formation. This inhibitory effect on OH also suppresses ozone formation near central Los Angeles. The main direct effect of lowering k_{1a} was a widespread OH increase (see Fig. S14b). Conversely, when k_{1a} was increased, OH decreased, as shown in Figure S14c. Changes in NO_2 (Fig. S15) were smaller in a relative sense, and varied in sign depending on location. We found little effect of changing k_{1a} on nitric acid concentrations in and around central Los Angeles. In this NO_2-rich area, there were offsetting effects of higher OH and lower k_{1a} on nitric acid formation. The reduction in k_{1a} led to small reductions (2-3%) in predicted nitric acid in downwind/inland areas (see Fig. S16b), where NO_2 faces greater competition from VOC in reacting with OH.

III. Figures and Legends

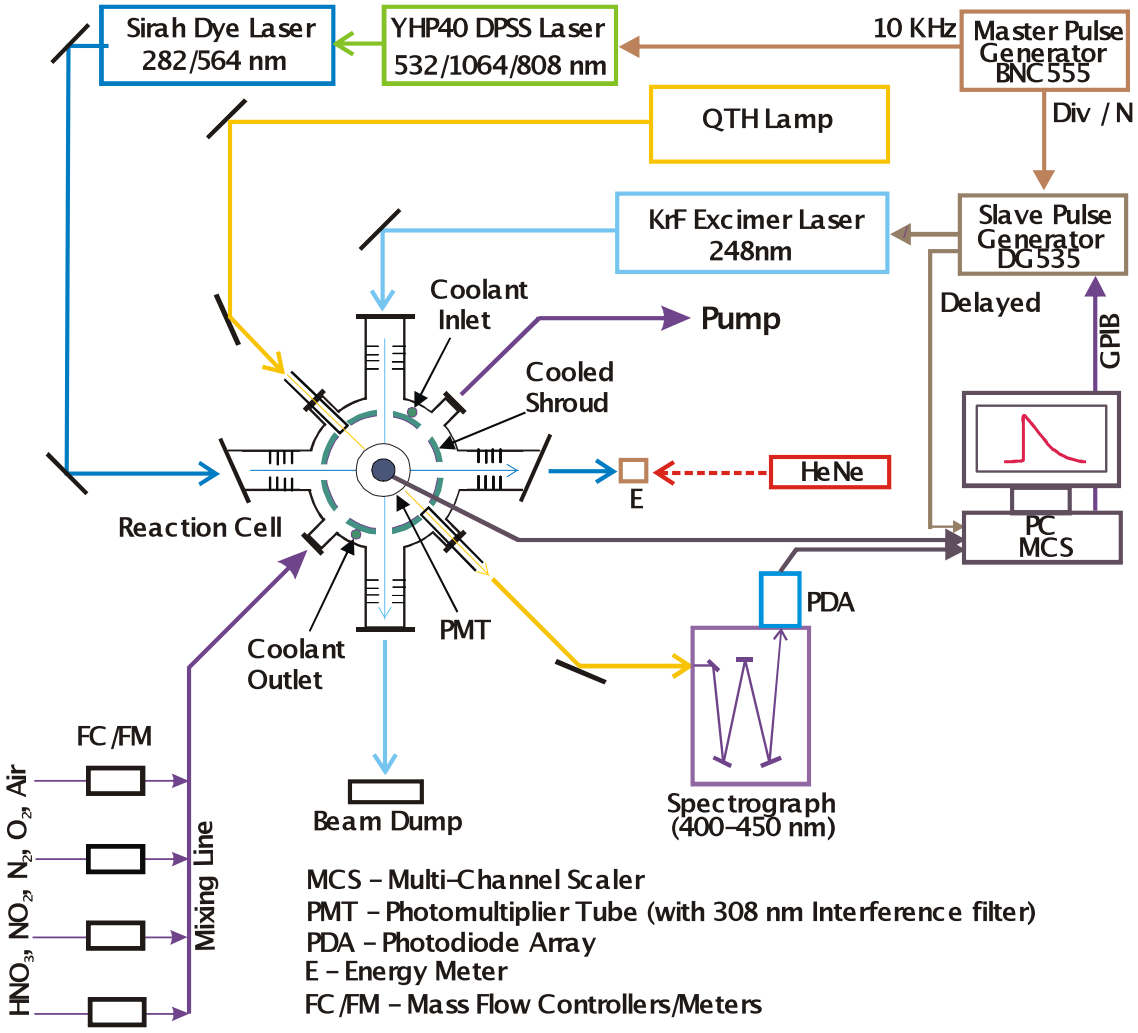

Fig. S1. Schematic diagram of the PLP-LIF system used to study the kinetics of OH + NO_2 + M at total buffer gas pressures of 20 - 900 Torr of air, N_2, O_2 and He.

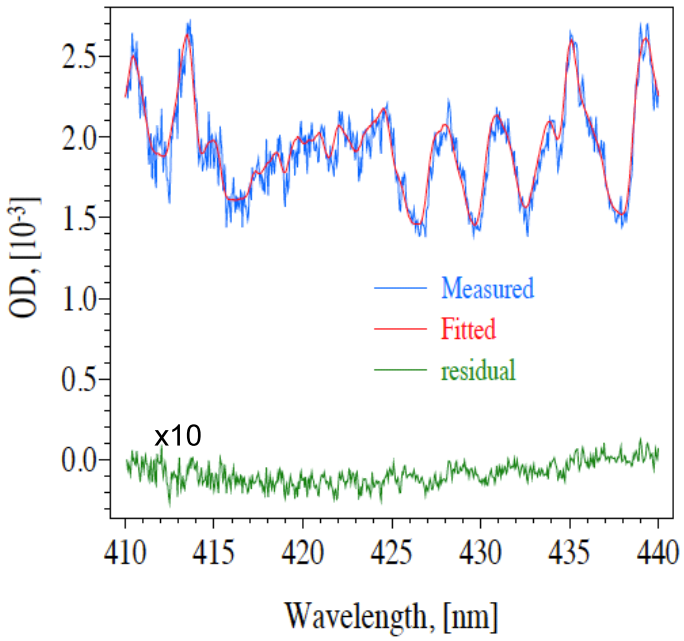

Fig. S2. Spectrum of NO_2 (3.49×10^{14} cm^{-3}) for a typical experiment from the in-situ absorption spectrometer. The optical path through the reactor is 10.0 cm. The upper curve shows the measured (blue) spectrum and a fit to the reference (red) spectrum. The green curve is the residual magnified by a factor of ten. OD = optical density.

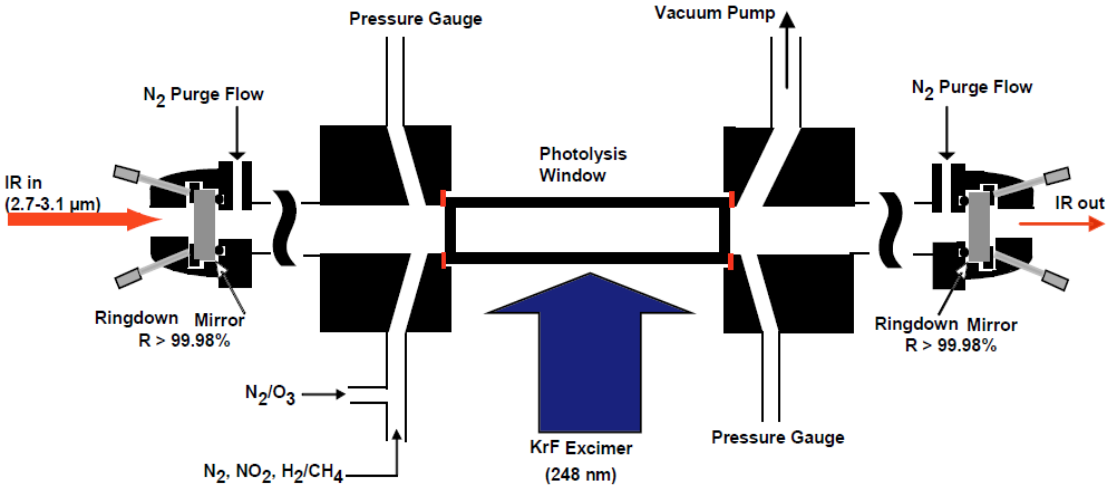

Fig. S3. Schematic of the Pulsed-Laser Photolysis-Cavity Ringdown Spectroscopy (PLP-CRDS) apparatus used for measurements of k_{1b}/k_{1a}.

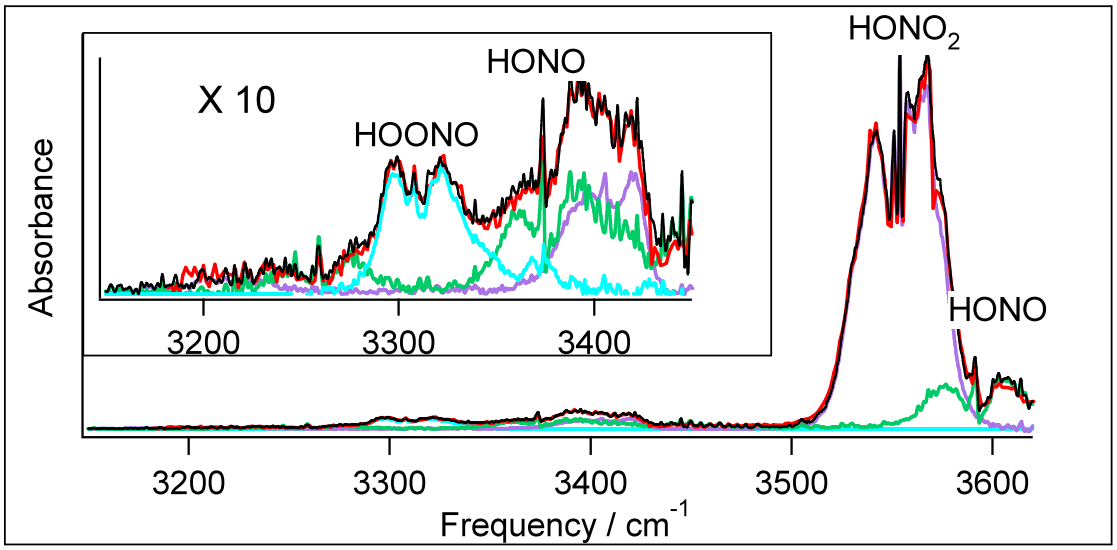

Fig. S4. Cavity Ringdown spectrum (black) of reaction products of OH + NO_2 taken with the PLP-CRDS apparatus. Data is compared to a fit with spectral components due to $HONO_2$ (purple), HONO (green), and HOONO (blue). The total fit is shown in red. The $HONO_2$ reference spectrum includes a frequency-dependent correction for nonlinearities in line shapes and intensities arising from the cavity ringdown method.

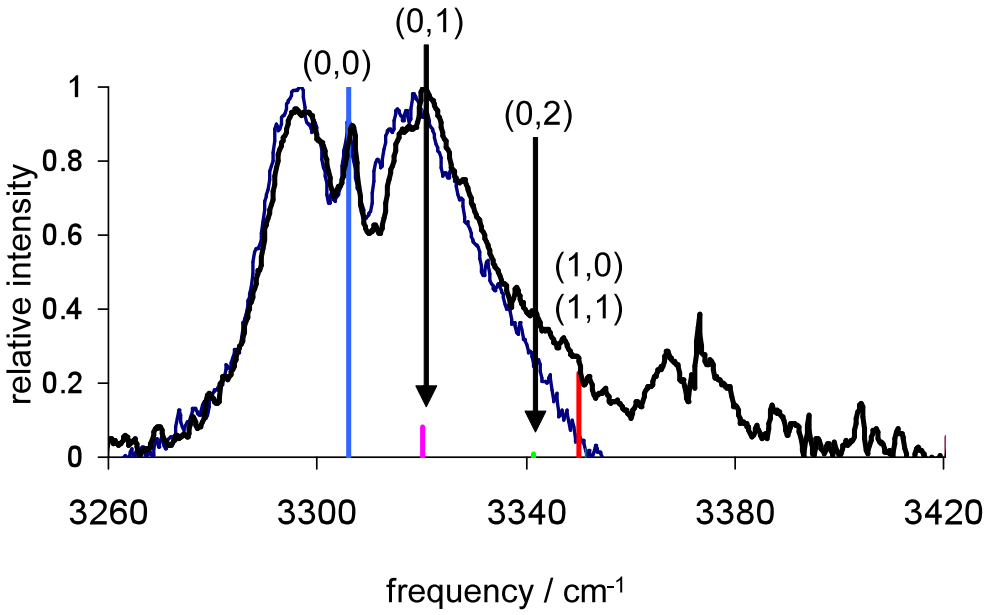

Fig. S5. Cavity Ringdown spectrum of the ν_1 (OH stretch) band of *cis-cis* HOONO (thick black) along with that previously reported (thin blue (*S10*)). Stick spectra are calculated positions and intensities of the origin and torsional hot bands which are identified by (n_{OONO}, n_{HOON}). This spectrum was used as the HOONO reference spectrum in fits of product spectra.

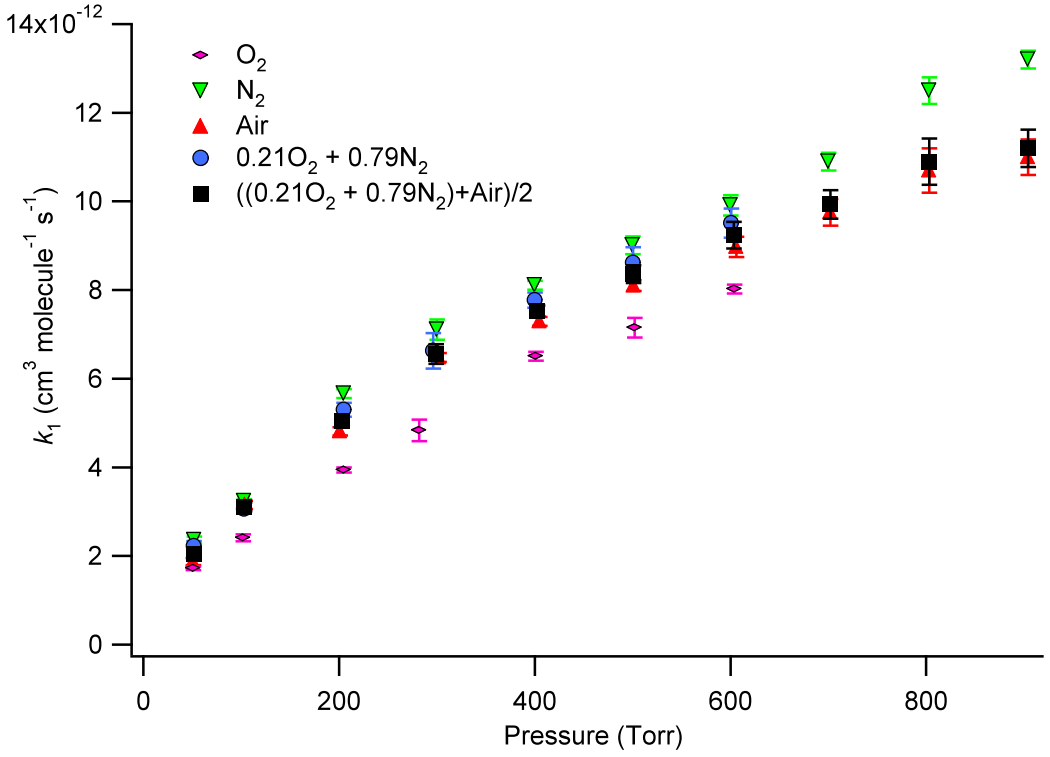

Fig. S6. Effective second order rate constants (k_1) for OH + NO_2 at 298K as a function of total pressure. Data were taken in buffer gases of O_2, N_2, and dry air. For comparison, the weighted linear combination of O_2 and N_2 are shown for comparison with the air data as well as the combined data (black squares) used for fitting. 2σ error bars shown represent random errors in the measurements.

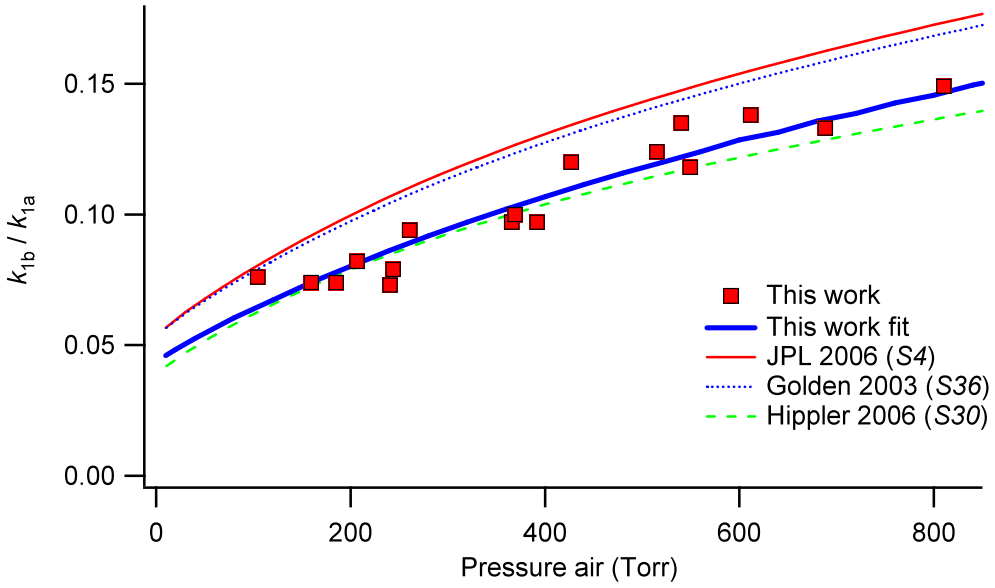

Fig. S7. The branching ratio $\alpha = k_{1b}/k_{1a}$ as a function of air pressure. Measurements with nitrogen concentrations >90% N_2 (red squares) and fit to this data. Previous recommendations in air at 298K are shown for comparison. The observed pressures have been scaled to give air pressure by assuming a relative collision efficiency for H_2 of $\beta = 0.67$ and for air of $\beta = 0.94$. The Golden 2003 and Hippler 2006 recommendations were in N_2 and the curves have similarly been scaled to give air pressure by assuming a relative collision efficiency for air of $\beta = 0.94$.

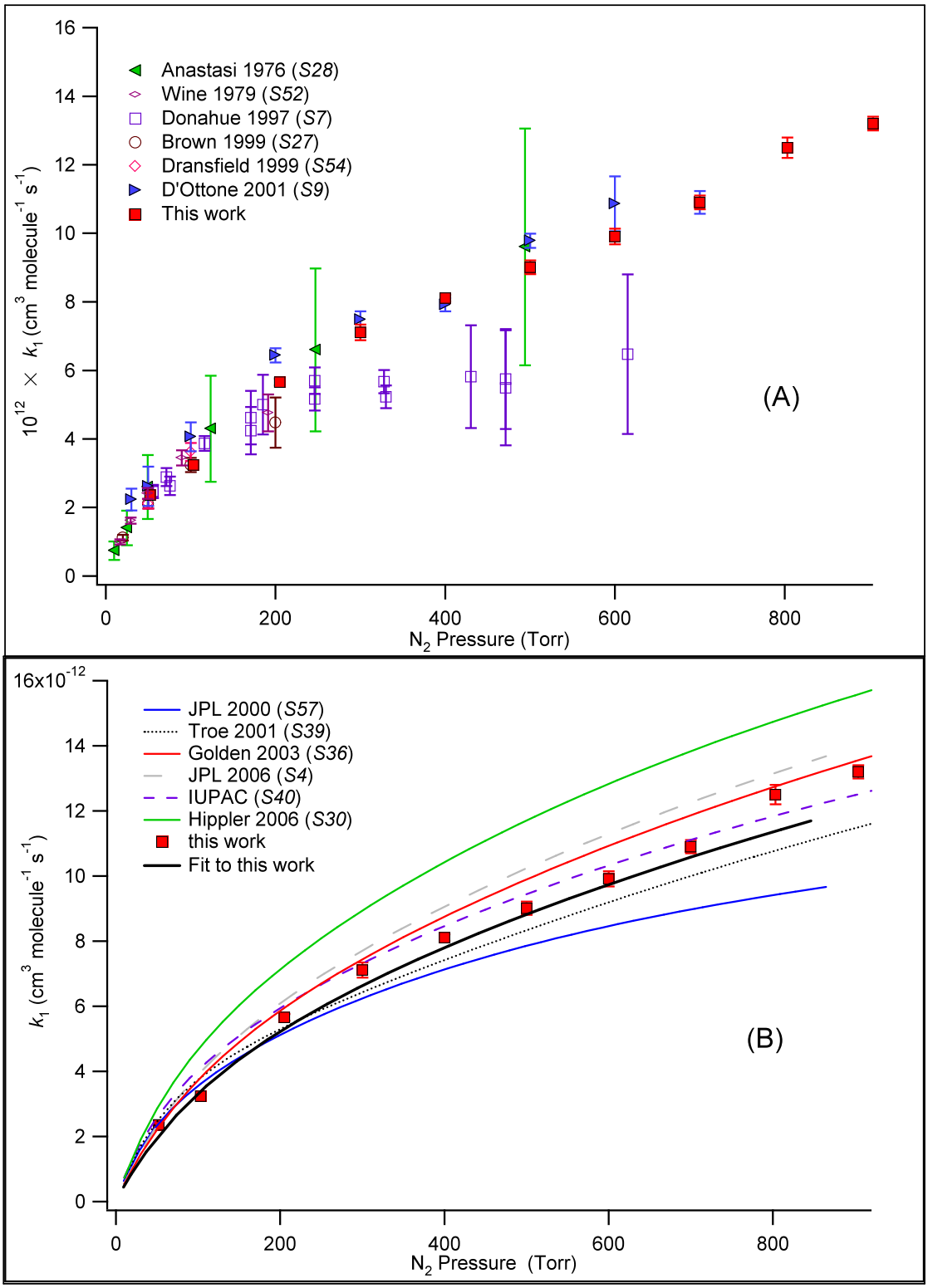

Fig. S8. (A) Comparison of data for the total rate constant k_1 taken in N_2 at 298K in this study to previous data. Uncertainties are 2σ. (B) Fall-off curves for k_1 along with our data in N_2 and our fit to our data. The abscissa for the calculated fall-off curves given in air (JPL, This work) were scaled to N_2 pressures using a relative collision efficiency for air of $\beta = 0.92$, $[N_2] = [\text{air}]/\beta$.

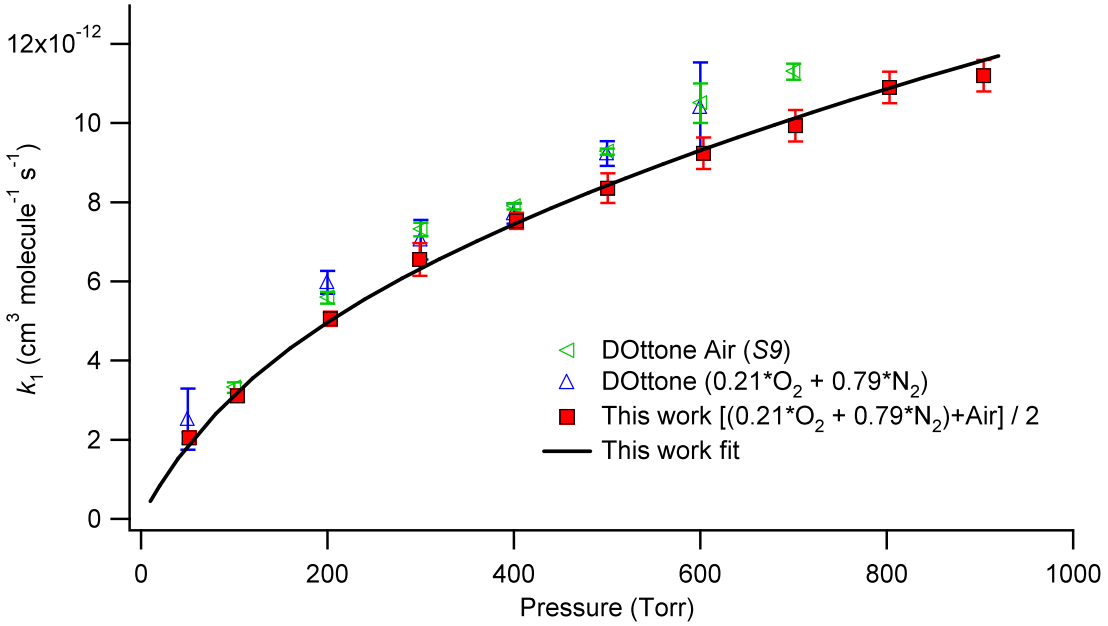

Fig. S9. Measurements of the total rate constant k_1 in air. The averaged data used for our fits to obtain fall-off parameters are shown as red squares. Uncertainties are 2σ. Results are compared to those of D'Ottone et al.

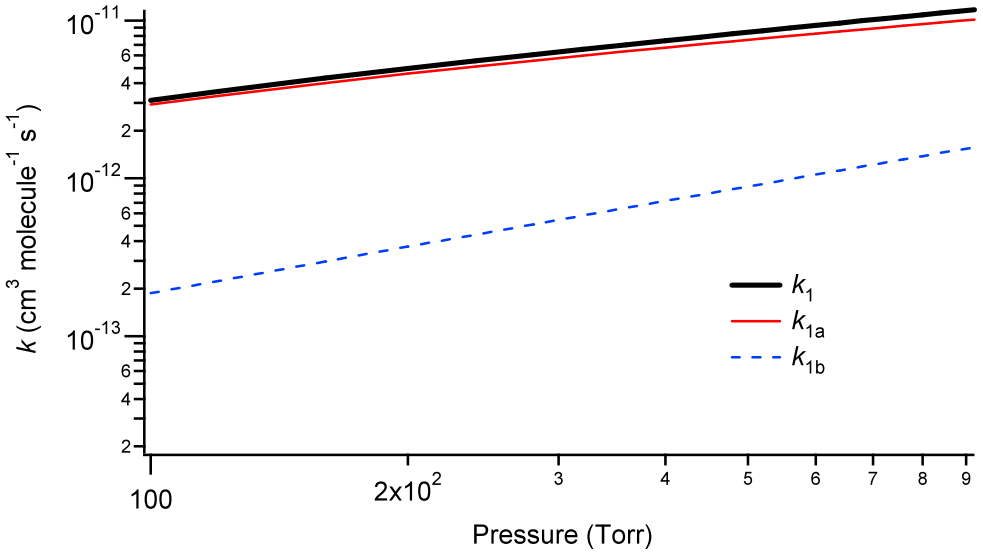

Fig. S10. Pressure dependence of the reaction rate coefficients for reactions 1, 1a, and 1b as determined from our fit to the data using the JPL formulation of the fall-off curves. Abscissa is pressure of air.

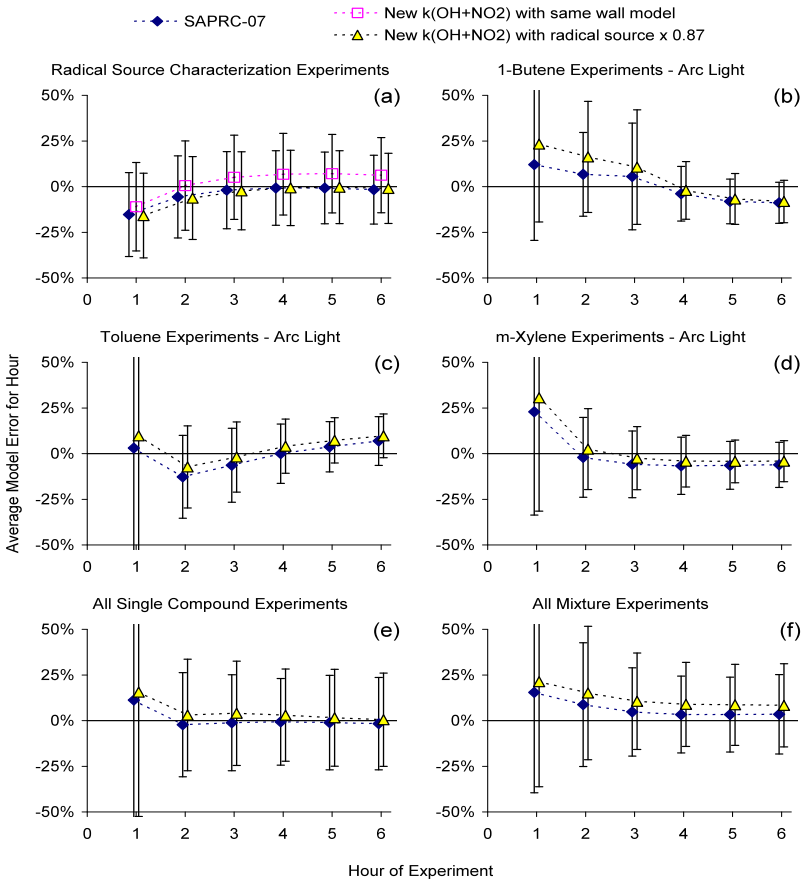

Fig. S11. Plots of average model errors vs. hour of experiment for selected experiments used to evaluate the SAPRC-07 mechanism.

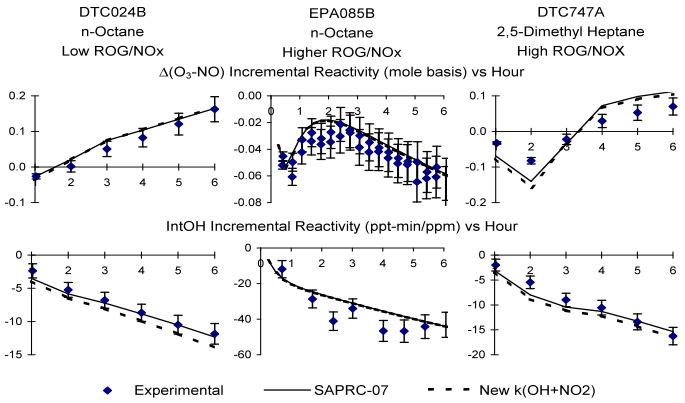

Fig. S12. Experimental and calculated $\Delta([O_3]–[NO])$ and IntOH incremental reactivities in selected representative incremental reactivity experiments used to evaluate alkane mechanisms.

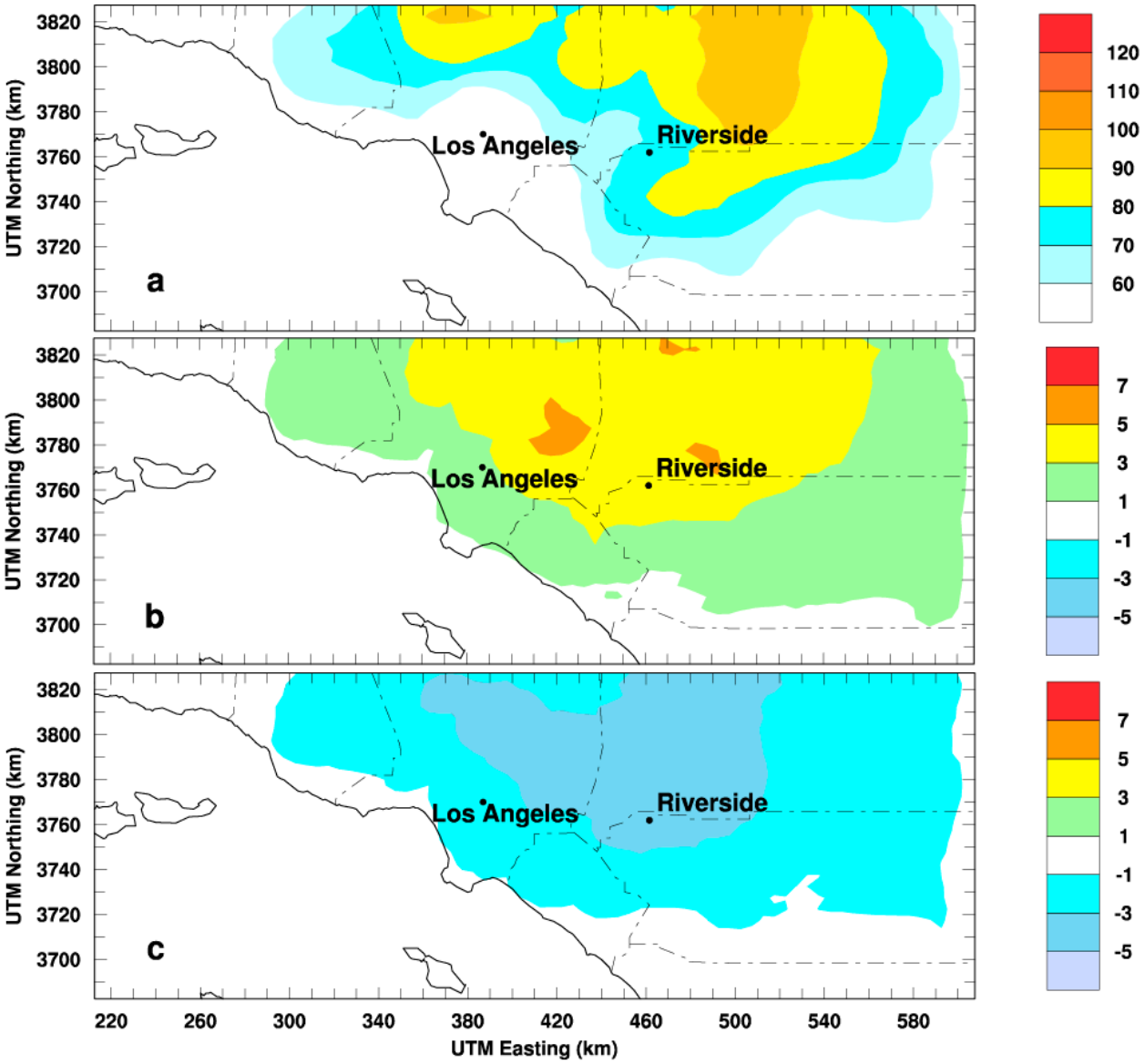

Fig. S13. Predicted summer peak 8-h average (0900-1700 h) ozone concentrations (ppb) in southern California using an Eulerian 3-D photochemical air quality model and emission inventory estimates for 2010. This figure is analogous to fig. 3 in the main text except that 8-h average ozone concentrations are shown here in contrast to 1-h midday values (1200-1300 h) in fig. 3. The base case (a) uses the SAPRC-07 mechanism (*S24*), which includes NASA/JPL 2006 (*S4*) recommendations for k_{1a}. The remaining panels show ozone differences in ppb relative to the base case: (b) uses the lower value of k_{1a} measured in this work, (c) uses the higher value of k_{1a} recommended by IUPAC (*S40*).

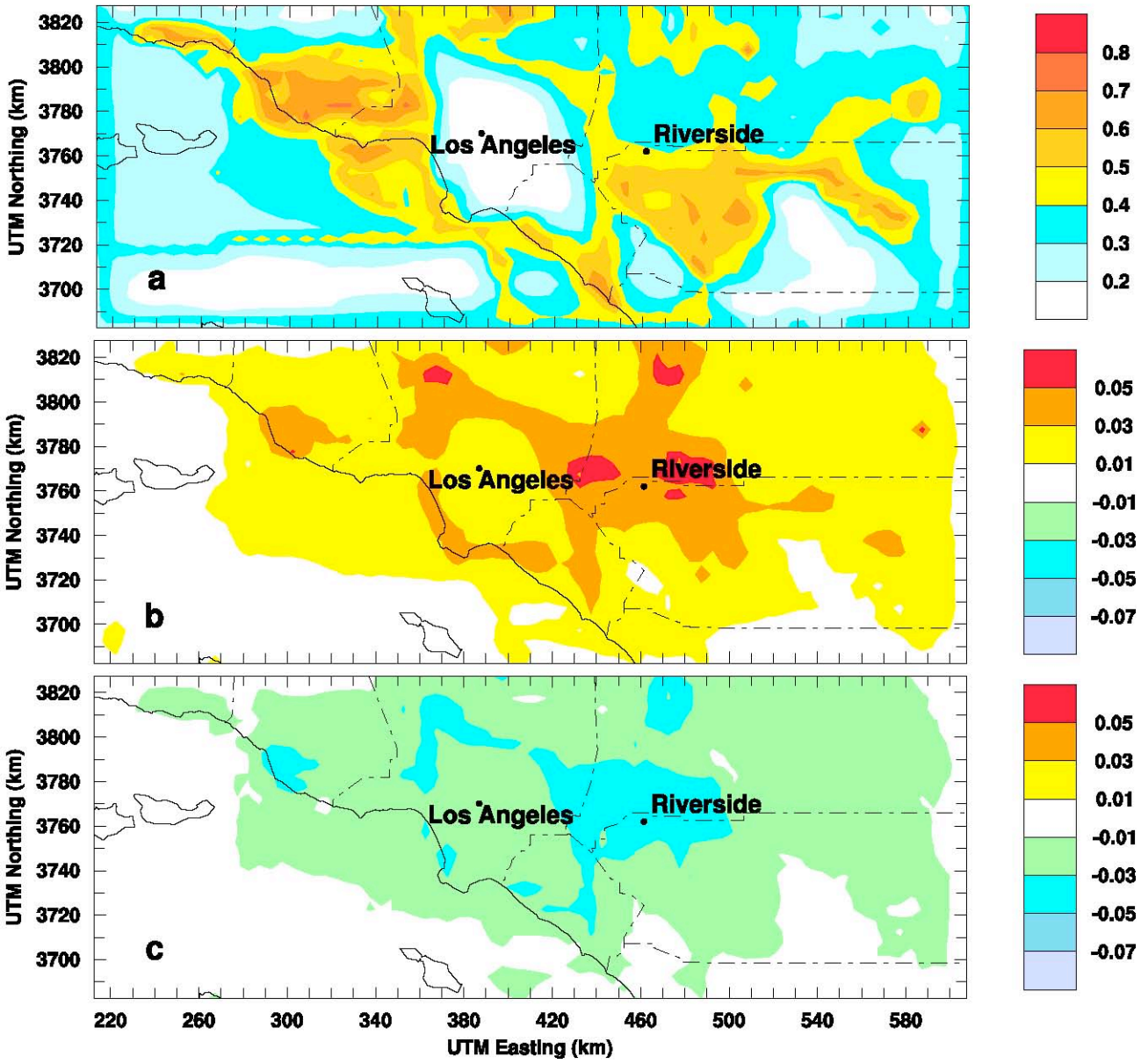

Fig. S14. Predicted midday (1200-1300 h) OH concentrations (ppt). The panels are as in fig. S13 but for 1-h OH.

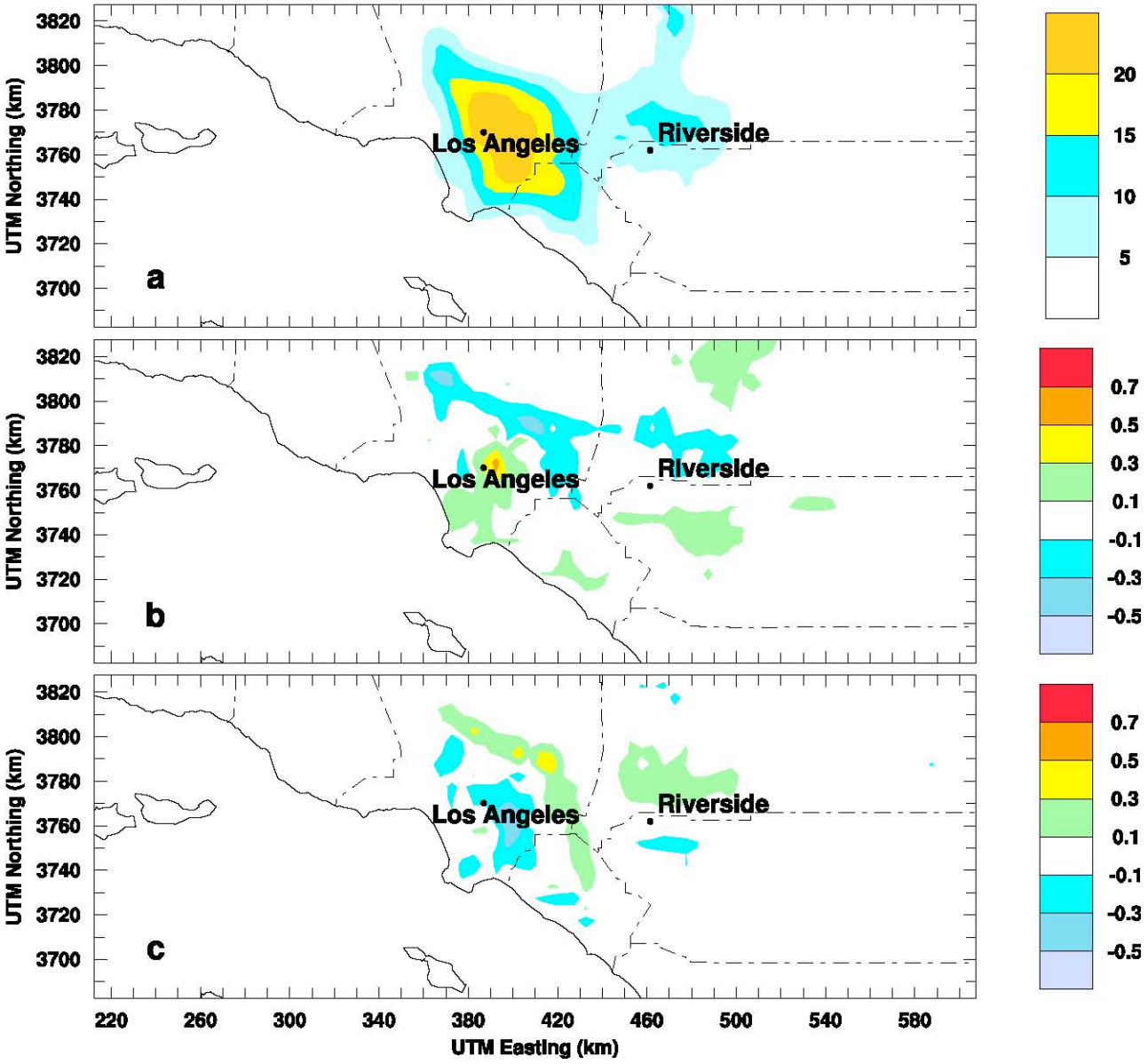

Fig. S15. Predicted midday (1200-1300 h) NO_2 concentrations (ppb). The panels are as in fig. S13 but for 1-h NO_2.

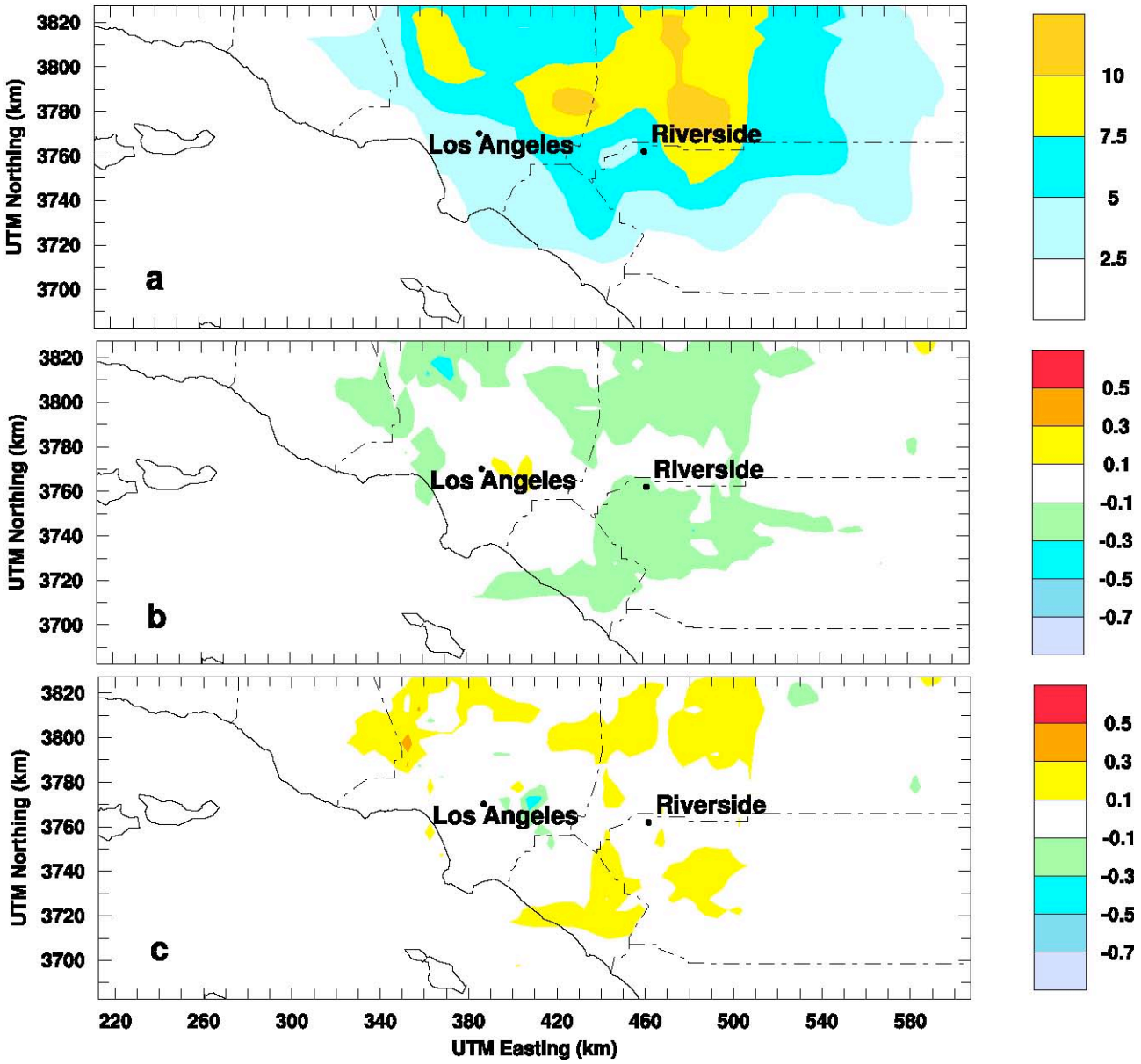

Fig. S16. Predicted midday (1200-1300 h) nitric acid concentrations (ppb). The panels are as in fig. S13 but for 1-h nitric acid.

IV. *Tables and Legends*

Table S1. Typical concentrations used in the OH kinetics experiments of the PLP-LIF apparatus and in the HOONO/$HONO_2$ branching ratio measurements using the PLP-IRCRDS apparatus.

PLP-LIF Experiment	
Gas	Concentration range / molecules cm^{-3}
OH	$(5\text{-}10)\times10^{10}$
NO_2	$(2\text{-}4)\times10^{14}$
$HONO_2$	1×10^{15}
O_2	Balance to total 2×10^{19}
air, N_2	balance to total 3×10^{19}
PLP-CRDS Experiment	
Gas	Concentration range / molecules cm^{-3}
OH	$(1\text{-}10)\times10^{13}$
O_3	$(1\text{-}10)\times10^{15}$
NO_2	$(1\text{-}10)\times10^{16}$
H_2	$(1\text{-}10)\times10^{17}$
N_2	balance to total (3.2-24) $)\times10^{18}$

Table S2. Partial list of calculated energies and frequencies for torsional hot bands of *cis-cis* HOONO. All energies and frequencies in cm^{-1}. Higher energy states all have individual relative populations less than 0.01 and a combined relative population of 0.036. States included in our experimental spectrum (Fig. S5) are in bold italics.

n_{HOON}	n_{OONO}	Energy $v_{OH} = 0$	$E-E_{000}$	relative population at 300 K	Energy $v_{OH} = 1$	transition freq	blue-shift
0	***0***	***2174.19***	***0.00***	***1.000***	***5546.25***	***3372.06***	***0.00***
1	***0***	***2481.65***	***307.45***	***0.227***	***5897.99***	***3416.35***	***44.29***
0	***1***	***2659.93***	***485.74***	***0.096***	***6046.14***	***3386.21***	***14.15***
2	0	2687.65	513.46	0.084	6174.41	3486.76	114.71
3	0	2767.79	593.60	0.057	6314.99	3547.19	175.14
4	0	2827.44	653.25	0.043	6396.30	3568.86	196.80
5	0	2924.94	750.75	0.027	6472.36	3547.42	175.36
1	***1***	***2940.52***	***766.33***	***0.025***	***6358.44***	***3417.92***	***45.86***
6	0	3022.74	848.55	0.017	6572.06	3549.32	177.26
2	1	3094.61	920.42	0.012	6611.61	3517.00	144.94
0	***2***	***3122.12***	***947.92***	***0.010***	***6529.22***	***3407.10***	***35.04***
7	0	3132.87	958.68	0.010	6679.30	3546.43	174.37

Table S3. Measurements of total rate coefficient k_1 in various bath gases at 298 K. Uncertanties are 1σ and reflect only random errors.

air		**O_2**		**N_2**		**$O_2N_2 = (0.21 \times O_2 + 0.79 \times N_2)$**		**Avg of air, O_2N_2***	
P (Torr)	$k_1 \times 10^{12}$ [cm^3 $molecule^{-1}$ s^{-1}]	P (Torr)	$k_1 \times 10^{12}$ [cm^3 $molecule^{-1}$ s^{-1}]	P (Torr)	$k_1 \times 10^{12}$ [cm^3 $molecule^{-1}$ s^{-1}]	P (Torr)	$k_1 \times 10^{12}$ [cm^3 $molecule^{-1}$ s^{-1}]	P (Torr)	$k_1 \times 10^{12}$ [cm^3 $molecule^{-1}$ s^{-1}]
51	1.87 ± 0.04	51	1.72 ± 0.02	52	2.36 ± 0.04	51.8	2.23± 0.03	51.4	2.05 ± 0.05
104	3.15 ± 0.05	102	2.41 ± 0.04	103	3.24 ± 0.02	102.8	3.06± 0.02	103.4	3.11 ± 0.05
201	4.81 ± 0.05	205	3.94 ± 0.03	205	5.66 ± 0.05	205	5.3± 0.04	203	5.05 ± 0.06
302	6.48 ± 0.05	282	4.83 ± 0.12	300	7.11 ± 0.12	296.2	6.63 ± 0.10	299.1	6.56 ± 0.11
405	7.29 ± 0.05	401	6.51 ± 0.05	400	8.11 ± 0.05	400.2	7.77 ± 0.04	402.6	7.53 ± 0.06
501	8.10 ± 0.06	502	7.15 ± 0.11	500	9.01 ± 0.10	500.4	8.62 ± 0.08	500.7	8.36 ± 0.10
606	8.97 ± 0.12	604	8.02 ± 0.05	600	9.91 ± 0.12	600.8	9.51 ± 0.09	603.4	9.24 ± 0.15
702	9.75 ± 0.15			700	10.9 ± 0.10			702	9.93 ± 0.19[a]
803	10.7 ± 0.25			803	12.5 ± 0.15			803	10.9 ± 0.28[a]
904	11.0 ± 0.20			904	13.2 ± 0.10			904	11.2 ± 0.23[a]

*. Values at three highest pressures have been estimated. See text.

Table S4. Summary of different experimental methods employed in previous studies of reaction (1) in the fall-off regime.
FP/RF - Flash Photolysis/Resonance Fluorescence
FP/RA - Flash Photolysis/Resonance Absorption
FP/LIF - Flash Photolysis/Laser Induced Fluorescence
PLP/LIF - Pulsed Laser Photolysis/Laser Induced Fluorescence
DF/LIF – High Pressure – Discharge Flow/Laser Induced Fluorescence
HP-DF/LIF – High Pressure – Discharge Flow/Laser Induced Fluorescence

Reference	Kinetic Techniques	P / Torr	Temp / K	Gases	$[NO_2]$ determination
Anastasi & Smith, 1976 (*S28*)	FP/RA	10 - 500	220 - 550	N_2, He, Ar, O_2, SF_6	Flow rate measurements of prepared NO_2 gas mixture
Wine et al, 1979 (*S52*)	FP/RF	14 - 700	247- 352	He, Ar, N_2, SF_6	External absorption cell (365nm)
Robertshaw and Smith, 1982 (*S53*)	FP/LIF	200 - 6000	295	Ar, CF_4	Gas dilution.
Donahue et al, 1997 (*S7*)	HP-DF/LIF	2 - 600	300	N_2	Absorption of a passive tracer diluted with gas mixtures (185nm)
Brown et al, 1999 (*S27*)	PLP/LIF	20 - 250	220 - 250	N_2, O_2	External absorption cell (365nm)
Dransfield et al, 1999 (*S54*)	DF-LIF	50 - 100	220 - 300	N_2	Absorption of a passive tracer diluted with gas mixtures (185nm)
D'Ottone et al, 2001 (*S9*)	PLP/LIF	30 - 700	273, 298	air, N_2,O_2,He	Absorption in reaction region + external absorption cell (365nm)
Hippler et al, 2002 (*S31*)	PLP/LIF	750 - 97500	300 - 480	He	External absorption cell (436 nm)
Hippler et al, 2006 (*S30*)	PLP/LIF	1500 - 375000	300 - 600	He/Ar	External absorption cell (436 nm)
Present work	PLP/LIF	50 - 900	298	air, N_2,O_2,He	Absorption in reaction region. Spectral fitting between 410 – 440nm

Table S5. Measurements and calculations of the product branching ratio $\alpha = k_{1b}/k_{1a}$. Previous results that report fractional yield have been converted to this ratio.

Article	Study	Gas	Pressure	Temp	α
Experiment					
This work	***CRDS / ab initio***	***Air***	***760 Torr****	***298 K***	***0.142 ± 0.012***
Burkholder, 1987 (*S55*)	FTIR spectroscopy	$He/N_2/SF_6$	3 - 850 Torr	248-298 K	< 0.11
Dransfield, 2001 (*S56*)	FTIR spectroscopy	>90% N_2	60 - 375 Torr	230 - 298 K	<0.11
Donahue, 2001 (*S29*)	isotope scrambling	N_2	k^0	298 K	0.17
Nizkorodov, 2002 (*S32*)	infrared overtone action spectroscopy	He/N_2	20 Torr	253 K	0.05 ± 0.03
Hippler, 2002 (*S31*)	OH + NO_2 Kinetics	He	3750 Torr	430 K	0.15
Bean 2003 Revised† (*S10*)	CRDS / ab initio	$He/Ar/N_2$	20 Torr	300 K	0.048 ± 0.013
D'Ottone, 2005 (*S8*)	isotope scrambling / kinetics	He	400 Torr	413 K	0.11 ± 0.03
Hippler, 2006 (*S30*)	OH + NO_2 kinetics / master equation	N_2	760 Torr	298 K	0.14
Theory					
Matheu, 2000 (*S38*)	modified strong collision, master equation	He	1000 Torr	300 K	0.10
Troe, 2001 (*S39*)	theory / fall-off analysis	N_2	760 Torr	298 K	<0.03
Zhu, 2003 (*S44*)	ab initio / RRKM	He	760 Torr	298 K	<0.03
Golden, 2003 (*S36*)	ab initio / master equation	N_2	760 Torr	298 K	0.17
Williams, 2007 (*S34*)	capture theory	N_2	20 Torr	300 K	0.051

*. The reported value reflects our fit value for α at 760 Torr of air. Experiments were performed in a mixture of predominantly N_2 (>90%) and H_2.

†. The published value of 0.075 ± 0.020 was revised in the current work based on improved knowledge of the $HONO_2$ nonlinearities, contributions from torsionally-excited HOONO, and ratio of $HOONO/HONO_2$ band intensities.

Table S6. Measurements of branching ratio α at 298 K in buffer gas containing N_2 (≥90%) and H_2.

P_{eff} N2((Torr)	Peff air† (Torr)	k1b / k1a
98	104	0.076
150	160	0.074
174	185	0.074
194	207	0.082
226	241	0.073
229	244	0.079
245	261	0.094
344	366	0.097
347	369	0.100
368	392	0.097
402	427	0.120
484	515	0.124
508	540	0.135
517	550	0.118
575	612	0.138
647	688	0.133
762	810	0.149

∗. Effective nitrogen pressure was obtained by assuming H_2 had a collisional efficiency of 0.67 relative to N_2, to account for the <10% hydrogen.
†. Effective air pressure was obtained by scaling the nitrogen pressure by $(0.94)^{-1}$.

Table S7. Fall-off parameters for reactions 1a and 1b in air or N_2 (as noted) at 298 K. Parameters from this work are not intended for use outside the range of pressures studied (100-800 Torr).

	k^0_{1a}	k^∞_{1a}	$F_{c,1a}$	k^0_{1b}	k^∞_{1b}	$F_{c,1b}$
This work (air)*	1.51×10^{-30}	2.58×10^{-11}	0.6	6.2×10^{-32}	8.1×10^{-11}	0.6
JPL 2006 (air) (*S4*)	1.84×10^{-30}	2.80×10^{-11}	0.6	9.3×10^{-32}	4.2×10^{-11}	0.6
IUPAC (N_2) (*S40*)	3.37×10^{-30}	4.10×10^{-11}	0.4			
Hippler 2006 (N_2) (*S30*)	2.5×10^{-30}	2.80×10^{-11}	0.62	9.4×10^{-32}	1.9×10^{-11}	0.73

$*$ - Fit only using measurements of α made with N_2 (>90%) and H_2.

References

S1. J. Troe, *J. Phys. Chem.* **83**, 114 (1979).
S2. K. Holbrook, M. Pilling, S. Robertson, *Unimolecular Reactions* (John Wiley and Sons, Inc., New York, ed. 2nd, 1996), pp. 10-18.
S3. P. Atkins, J. de Paula, *Physical Chemistry* (W. H. Freeman and Company, New York, ed. Seventh, 2002), pp. 890-891.
S4. S. P. Sander *et al.*, "Chemical Kinetics and Photochemical Data for Use in Atmospheric Studies, Evaluation Number 15" *JPL Publication 06-2* (Jet Propulsion Laboratory, California Institute of Technology, Pasadena, CA, 2006; http:\\jpldataeval.jpl.nasa.gov/pdf/JPL_15_AllInOne.pdf).
S5. A. C. Vandaele *et al.*, *J. Atmos. Chem.* **25**, 289 (1996).
S6. S. A. Nizkorodov, S. P. Sander, L. R. Brown, *J. Phys. Chem. A* **108**, 4864 (2004).
S7. N. M. Donahue, M. K. Dubey, R. Mohrschladt, K. L. Demerjian, J. G. Anderson, *J. Geophys. Res.-Atmospheres* **102**, 6159 (1997).
S8. L. D'Ottone, D. Bauer, P. Campuzano-Jost, M. Fardy, A. J. Hynes, *Faraday Discuss.* **130**, 111 (2005).
S9. L. D'Ottone, P. Campuzano-Jost, D. Bauer, A. J. Hynes, *J. Phys. Chem. A* **105**, 10538 (2001).
S10. B. D. Bean *et al.*, *J. Phys. Chem. A* **107**, 6974 (2003).
S11. S. A. Reid, Y. Tang, *Appl. Opt.* **35**, 1473 (1996).
S12. J. L. Fry *et al.*, *J. Chem. Phys.* **121**, 1432 (2004).
S13. I. W. Smith, M. D. Williams, *J. Chem. Soc.-Faraday Trans. II* **81**, 1849 (1985).
S14. C. R. Park, J. R. Wiesenfeld, *J. Chem. Phys.* **95**, 8166 (1991).
S15. P. M. Aker, J. J. Sloan, *J. Chem. Phys.* **85**, 1412 (1986).
S16. X. Zhang, M. R. Nimlos, G. B. Ellison, M. E. Varner, J. F. Stanton, *J. Chem. Phys.* **124** (2006).
S17. K. J. Feierabend, D. K. Havey, M. E. Varner, J. F. Stanton, V. Vaida, *J. Chem. Phys.* **124** (2006).
S18. J. Matthews, A. Sinha, *J. Chem. Phys.* **122** (2005).
S19. A. B. McCoy, J. L. Fry, J. S. Francisco, A. K. Mollner, M. Okumura, *J. Chem. Phys.* **122**, 104311 (2005).
S20. A. B. McCoy, M. K. Sprague, M. Okumura, *J. Phys. Chem. A* **114**, 1324 (2010).
S21. E. X. J. Li, I. M. Konen, M. I. Lester, A. B. McCoy, *J. Phys. Chem. A* **110**, 5607 (2006).
S22. W. P. L. Carter, "Development of the SAPRC-07 chemical mechanism and updated ozone reactivity scales." (Report to the California Air Resources Board, 2007; http://www.cert.ucr.edu/ftp/pub/carter/SAPRC).
S23. W. P. L. Carter, "Development of the SAPRC-07 Chemical Mechanism", *Atmos. Environ.* doi:10.1016/j.atmosenv.2010.01.026, (2010).
S24. W. P. L. Carter, "Development of a Condensed SAPRC-07 Chemical Mechanism" (Final Report to the California Air Resources Board, 2009; http://www.cert.ucr.edu/~carter/absts.htm#csaprc07).
S25. W. P. L. Carter, F. W. Lurmann, *Atmos. Environ. A* **25**, 2771 (1991).

S26. W. P. L. Carter, R. Atkinson, A. M. Winer, J. N. Pitts, *Int. J. Chem. Kinet.* **14**, 1071 (1982).
S27. S. S. Brown, R. K. Talukdar, A. R. Ravishankara, *Chem. Phys. Lett.* **299**, 277 (1999).
S28. C. Anastasi, I. W. M. Smith, *J. Chem. Soc.-Faraday Trans. II* **72**, 1459 (1976).
S29. N. M. Donahue, R. Mohrschladt, T. J. Dransfield, J. G. Anderson, M. K. Dubey, *J. Phys. Chem. A* **105**, 1515 (2001).
S30. H. Hippler, N. Krasteva, S. Nasterlack, F. Striebel, *J. Phys. Chem. A* **110**, 6781 (2006).
S31. H. Hippler, S. Nasterlack, F. Striebel, *Phys. Chem. Chem. Phys.* **4**, 2959 (2002).
S32. S. A. Nizkorodov, P. O. Wennberg, *J. Phys. Chem. A* **106**, 855 (2002).
S33. I. M. Konen *et al.*, *J. Chem. Phys.* **122** (2005).
S34. C. F. Williams, S. K. Pogrebnya, D. C. Clary, *J. Chem. Phys.* **126** (2007).
S35. D. Chakraborty, J. Park, M. C. Lin, *Chem. Phys.* **231**, 39 (1998).
S36. D. M. Golden, J. R. Barker, L. L. Lohr, *J. Phys. Chem. A* **107**, 11057 (2003).
S37. D. M. Golden, G. P. Smith, *J. Phys. Chem. A* **104**, 3991 (2000).
S38. D. M. Matheu, W. H. Green, *Int. J. Chem. Kinet.* **32**, 245 (2000).
S39. J. Troe, *Int. J. Chem. Kinet.* **33**, 878 (2001).
S40. R. Atkinson *et al.*, "Summary of evaluated kinetic and photochemical data for atmospheric chemistry" (IUPAC subcommittee on gas kinetic data evaluation for atmospheric chemistry, 2006; http://www.iupac-kinetic.ch.cam.ac.uk/).
S41. J. Y. Zhang, N. M. Donahue, *J. Phys. Chem. A* **110**, 6898 (2006).
S42. D. A. Dixon, D. Feller, C. G. Zhan, J. S. Francisco, *J. Phys. Chem. A* **106**, 3191 (2002).
S43. Y. D. Liu, R. G. Zhong, *J. Mol. Struct.-Theochem.* **765**, 143 (2006).
S44. R. S. Zhu, M. C. Lin, *J. Chem. Phys.* **119**, 10667 (2003).
S45. R. Sumathi, S. D. Peyerimhoff, *J. Chem. Phys.* **107**, 1872 (1997).
S46. Y. L. Zhao, K. N. Houk, L. P. Olson, *J. Phys. Chem. A* **108**, 5864 (2004).
S47. Y. Liu, L. L. Lohr, J. R. Barker, *J. Phys. Chem. A* **110**, 1267 (2006).
S48. C. Chen, B. C. Shepler, B. J. Braams, J. M. Bowman, *J. Chem. Phys.* **127**, 104310 (2007).
S49. C. Chen, B. C. Shepler, B. J. Braams, J. M. Bowman, *Phys. Chem. Chem. Phys.* **11**, 4722 (2009).
S50. W. P. L. Carter, *Atmos. Environ.* **29**, 2513 (1995).
S51. W. P. L. Carter, R. Atkinson, *Environ. Sci. Tech.* **21**, 670 (1987).
S52. P. H. Wine, N. M. Kreutter, A. R. Ravishankara, *J. Phys. Chem.* **83**, 3191 (1979).
S53. J. S. Robertshaw, I. W. M. Smith, *J. Phys. Chem.* **86**, 785 (1982).
S54. T. J. Dransfield *et al.*, *Geophys. Res. Lett.* **26**, 687 (1999).
S55. J. B. Burkholder, P. D. Hammer, C. J. Howard, *J. Phys. Chem.* **91**, 2136 (1987).
S56. T. J. Dransfield, N. M. Donahue, J. G. Anderson, *J. Phys. Chem. A* **105**, 1507 (2001).
S57. S. P. Sander *et al.*, "Chemical Kinetics and Photochemical Data for Use in Stratospheric Modeling Supplement to Evaluation 12: Update of Key Reactions, Evaluation Number 13" *JPL Publication 00-3* (Jet Propulsion Laboratory, California Institute of Technology, Pasadena, CA, 2000; http:\\jpldataeval.jpl.nasa.gov/pdf/JPL_00-03.pdf).